MAX-DOAS observations of formaldehyde and nitrogen dioxide at three sites in Asia and comparison with the global chemistry transport model CHASER

Hossain Mohamed Syedul Hoque[1], Kengo Sudo[1,2], Hitoshi Irie[3], Alessandro Damiani[3], Manish Naja[4], and Al Mashroor Fatmi[3]

[1]Graduate School of Environmental Studies, Nagoya University, Nagoya, 4640064, Japan

[2]Japan Agency for Marine-Earth Science and Technology (JAMSTEC), Kanagawa, 2370061, Japan

[3]Center for Environmental Remote Sensing (CEReS), Chiba University, Chiba,2638522, Japan

[4]Aryabhatta Research Institute for Observational Sciences (ARIES), Manora Peak, Nainital-263001, Uttarakhand, India

Correspondence to: Hossain Mohammed Syedul Hoque (hoque.hossain.mohammed.syedul.u6@f.mail.nagoya-u.ac.jp or hoquesyedul@gmail.com)

Abstract. Formaldehyde (HCHO) and nitrogen dioxide (NO_2) concentrations and profiles were retrieved from ground-based multi-axis differential optical absorption spectroscopy (MAX-DOAS) observations during January 2017 - December 2018 at three sites in Asia: (1) Phimai (15.18°N, 102.5°E), Thailand; (2) Pantnagar (29°N, 78.90°E) in the Indo Gangetic Plain (IGP), India; and (3) Chiba (35.62°N, 140.10°E), Japan. Retrievals were performed using the Japanese MAX-DOAS profile retrieval algorithm ver. 2 (JM2). The observations were used to evaluate the NO_2 and HCHO partial columns and profiles (0 - 4 km) simulated using the global chemistry transport model (CTM) CHASER. The NO_2 and HCHO concentrations at all three sites showed consistent seasonal variation throughout the investigated period. Biomass burning affected the HCHO and NO_2 variations at Phimai during the dry season and at Pantnagar during spring (March - May) and post-monsoon (September - November). Results found for the HCHO to NO_2 ratio (R_{FN}), an indicator of high ozone sensitivity, indicate that the transition region (i.e., $1 < R_{FN} < 2$) changes regionally, echoing the recent finding for R_{FN} effectiveness. Moreover, reasonable estimates of transition regions can be derived, accounting for the NO_2 - HCHO chemical feedback.

28 The model was evaluated against global NO_2 and HCHO columns data retrieved from Ozone Monitoring

29 Instrument (OMI) observations before comparison with ground-based datasets. Despite underestimation,

30 the model well simulated the satellite-observed global spatial distribution of NO_2 and HCHO, with

31 respective spatial correlations (*r*) of 0.73 and 0.74. CHASER demonstrated good performance,

32 reproducing the MAX-DOAS retrieved HCHO and NO_2 abundances at Phimai, mainly above 500 m from

33 the surface. Model results agree with the measured variations within the one sigma standard deviation of

34 the observations. Simulations at higher resolution improved the modeled NO_2 estimates for Chiba,

35 reducing the mean bias error (MBE) for the 0 - 2 km height by 35%, but resolution-based improvements

36 were limited to surface layers. Sensitivity studies show that at Phimai, pyrogenic emissions contribute to

37 HCHO and NO_2 concentrations up to 50 and 35%, respectively.

1 Introduction

39 Formaldehyde (HCHO), the most abundant carbonyl compound in the atmosphere, is a high-yield product

40 of oxidization of all primary volatile organic compounds (VOCs) emitted from natural and anthropogenic

41 sources by hydroxyl radicals (OH). Oxidation of long-lived VOCs such as methane produces a global

42 HCHO background concentration of 0.2 – 1.0 ppbv in remote marine environments (Weller et al., 2000;

43 Burkert et al., 2001; Singh et al., 2004; Sinreich et al., 2005). Aside from oxidation of VOCs, the

44 significant sources of HCHO are direct emissions from biomass burning, industrial processes, fossil fuel

45 combustion (Lee et al., 1997; Hak et al., 2005; Fu et al., 2008), and vegetation (Seco et al., 2007).

46 However, oxidization of non-methane VOCs emitted from biogenic (e.g., isoprene) or anthropogenic (e.g.,

47 butene) sources govern the spatial variation of HCHO on a global scale (Franco et al., 2015). The sinks

48 of HCHO include photolysis at wavelengths shorter than 400 nm, oxidation by OH, and wet deposition,

49 thereby limiting the lifetime of HCHO to a few hours (Arlander et al., 1995).

50 Nitrogen dioxide (NO_2), an important atmospheric constituent, (1) participates in the catalytic

51 formation of tropospheric ozone (O_3), (2) acts as a catalyst for stratospheric ozone (O_3) destruction

52 (Crutzen, 1970), (3) contributes to the formation of aerosols (Jang and Kamens, 2001), (4) acts as a

53 precursor of acid rain (Seinfeld and Pandis, 1998), and (5) strongly affects radiative forcing (Solomon et

54 al. 1999; Lelieved et al., 2002;). Nitrogen oxides (NO_x = NO (nitric oxide) + NO_2) are emitted from

55 natural and anthropogenic sources. Primary NO_x emission sources include biomass burning, fossil fuel

combustion, soil emissions, and lightning (Bond et al., 2001; Zhang et al., 2003). Not only do NO_x emissions degrade air quality; they are leading air pollutant (Ma et al., 2013). Both HCHO and NO_2 are important intermediates in the global VOC–HO_x (hydrogen oxides)–NO_x catalytic cycle, which governs O_3 chemistry in the troposphere (Lee et al., 1997; Houweling et al., 1998; Hak et al., 2005; Kanakidou et al., 2005). Thus, both trace gases play crucially important roles in tropospheric chemistry.

The observational sites examined for the present study have different atmospheric characteristics. Thailand is strongly affected by pollution because of rapid economic development and urbanization. Moreover, biomass burning in Southeast Asia is a significant source of O_3 precursors, contributing up to 30% of the total concentrations during the peak burning season (Amnuaylorajen et al., 2020; Khodmanee et al. 2021). Because of rapid industrialization, India the second most populous country in the world, is witnessing an increasing O_3 trend along with NO_2 and HCHO concentrations in all major cities (Mahajan et al; 2015; Lu et al, 2018;). The Indo-Gangetic Plain (IGP), which covers ~21% of the Indian subcontinent land area is hotspots of severe air pollution (Giles et al; 2005, Biswas et al; 2019). In contrast, surface O_3 concentrations have shown an increasing trend in Japan, despite decreasing NO_x and VOC concentrations related to emission control measures after 2000 (Irie et al., 2021). Therefore, observational and modeling studies must be conducted to improve our quantitative understanding of the O_3-NO_x-VOC relation in these regions.

Multi-axis differential optical absorption spectroscopy (MAX-DOAS), a well-established, unique, and powerful remote sensing method for measuring trace gases and aerosols, is based on the DOAS technique. Aerosols and trace gases are quantified using selective narrowband (high frequency) absorption features (Platt 1994; Platt and Stutz 2008). Spectral radiance measurements at different elevation angles (ELs) can provide profile information about atmospheric trace gases and aerosols (Hönninger et al., 2004; Wagner et al., 2004; Wittrock et al., 2004; Frieß et al., 2006; Irie et al., 2008a). Many studies have demonstrated the retrieval of aerosol and trace gas concentrations and profiles from MAX-DOAS observations, including NO_2 and HCHO (Clémer et al., 2010; Irie et al., 2011; Hendrick et al., 2014; Wang et al., 2014; Franco et al., 2015; Frieß et al., 2016).

The ability of MAX-DOAS to provide information related to surface concentrations, vertical profiles, and column densities makes it a good complement to ground-based in situ and satellite observations.

Moreover, the MAX-DOAS method uses narrowband absorption of the target compounds, thereby obviating any need for radiometric calibration of the instrument. Because of these advantages, MAX-DOAS systems are deployed for the assessment of aerosol and trace gases in regional and global observational networks such as BREDOM (Wittrock et al., 2004), BIRA-IASB (Clémer et al., 2010), and MADRAS (Kanaya et al., 2014). Such datasets are used, in but are not limited to, (1) air quality assessment and monitoring, (2) evaluation of chemistry-transport models (CTMS), and (3) validation of satellite data retrievals. Several studies have used MAX-DOAS datasets to validate tropospheric columns retrieved from satellite observations, including NO_2 and HCHO (Irie et al., 2008b; Ma et al., 2013; Chan et al., 2020; Ryan et al., 2020). However, limited MAX-DOAS datasets have been used to evaluate global CTMs. Vigouroux et al. (2009) and Franco et al. (2015) respectively used the MAX-DOAS HCHO datasets from Reunion Island and Jungfraujoch stations to evaluate the Intermediate Model of Annual and Global Evolution of Species (IMAGES) and GEOS-Chem model simulations. Kanaya et al. (2014) validated the Model for Interdisciplinary Research on Climate–Earth System Model – Chemistry (MIROC-ESM-CHEM) simulated NO_2 column densities with MAX-DOAS observations in Cape Hedo and Fukue in Japan. Kumar et al. (2021) used MAX-DOAS observations to evaluate the high-resolution regional model Meco(n)(MESSy-field ECHAM and COSMO model nested n times).

For this study, NO_2 and HCHO profiles retrieved from MAX-DOAS observations from the International air quality and sky research remote sensing (A-SKY) (http://atmos3.cr.chiba-u.jp/a-sky/) network sites are used to evaluate the global Chemical Atmospheric General Circulation Model for the Study of Atmospheric Environment and Radiative Forcing (CHASER; Sudo et al., 2002). The three A-SKY sites of - (1) Phimai in Thailand (15.18°N, 102.56°E), (2) Pantnagar (29°N, 78.90°E) in the IGP in India, and (3) Chiba (35.62°N, 140.10°E) in Japan, are respectively representative of rural, semi-rural, and urban environments. CHASER has been used mostly for global-scale research (Sudo et al., 2007; Sekiya et al., 2014, 2018; Miyazaki et al., 2017). The study described herein is the first reported attempt to evaluate the CHASER-simulated NO_2 and HCHO profiles using MAX-DOAS observations in three different atmospheric environments. Moreover, few reports of the literature have described the use of MAX-DOAS datasets to evaluate global CTMs in South Asia and South-east Asia. Overall, this study was conducted

to provide important insights into model performances and to help reduce model uncertainties related to NO$_2$ and HCHO simulations in these regions.

The paper is structured in the following manner. First, the observation sites, MAX-DOAS instrumentation, and retrieval strategies are described in section 2. Section 2 also includes a short description of the CHASER model and Ozone Monitoring Instrument (OMI) HCHO and NO$_2$ retrievals. Next, the observations and the evaluation results are described in sections 3. Finally, the sensitivity study results are provided in section 3.4. and the concluding remarks in section 4.

2 Observations, datasets, and methods

2.1 Site Information

Continuous MAX-DOAS observations at Chiba, Phimai, and Pantnagar started respectively in 2012, 2014, and 2017. The measurements from January 2017 to December 2018 at all three sites are discussed herein. Phimai, a rural site, is located ~260 km north-east of the Bangkok metropolitan area and is unlikely to be affected by vehicular and industrial emissions. However, the site is affected by biomass burning during January - April. Two major air streams: the dry, cool north-east monsoon during November – mid-February and the wet, warm south-west monsoon during mid-May – September affect the climate in Phimai. As described by, Hoque et al. (2018), the climate classifications of Phimai are the (a) dry season (January – April), and (b) wet season (June – September).

Pantnagar, a semi-urban site in India, is located in the IGP. The Indian capital of New Delhi is situated at ~225 km south-west of the site. The low-altitude plains are on the south and west sides of the site. The Himalayan mountains are located to the north and east. An important roadway with moderate traffic volume and a small local airport lies within 3 km of the site. Rudrapur (~12 km south-west of Pantnagar) and Haldwani (~ 25 km north-east of Pantnagar) are the two major cities near Pantnagar, where non-combustible industries are located (Joshi et al., 2016). The climate classification at Pantnagar is the

137 following: (1) winter (December–February), (2) spring (March-May), (3) summer monsoon (June–
138 August), and (4) autumn (September–November).

139   Chiba, an urban site, is located ~40 km south-east of the Tokyo metropolitan region. Tokyo Bay,
140 large-scale industries, and residential areas are located within a 50 km radius. Chiba has four distinct
141 seasons: (1) spring (March-May), (2) summer (June–August), (3) autumn (September–November), and
142 winter (December– February). The locations of the three sites are depicted in Fig. 1.

143

144
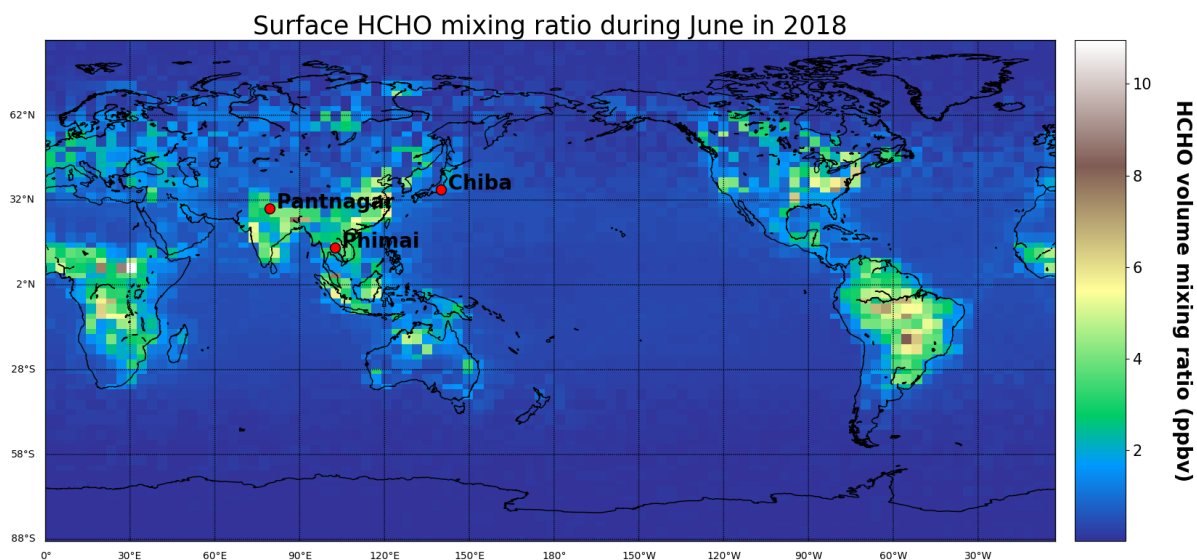
145 **Figure 1:** Surface HCHO mixing ratio in June 2018, simulated using the CHASER model. The red points
146 represent the locations of the observation sites, which are part of the A-SKY network.

147

148

2.2 MAX-DOAS retrieval

The MAX-DOAS systems used for continuous observations at the three sites participated in the Cabauw Intercomparison Campaign of Nitrogen Dioxide measuring Instruments (CINDI) (Roscoe et al., 2010) and CINDI-2 (Kreher et al., 2020) campaigns. The instrumentation setup is described by Irie et al. (2008, 2011, 2015). The indoor part of the MAX-DOAS systems consists of an ultraviolet-visible (UV-VIS) spectrometer (Maya2000Pro; Ocean Optics Inc.) embedded in a temperature-controlled box. The outdoor unit consists of a single telescope and a 45° inclined movable mirror on a rotary actuator, used to perform reference and off-axis measurements. The high-resolution spectra from 310–515 nm is recorded at six elevation angles (ELs) of 2°, 3°, 4°, 6°, 8°, and 70° at the Chiba and Phimai sites. At the Pantnagar site, measurements are conducted at ELs of 3°, 4°, 5°, 6°, 8°, and 70°. The sequences of the ELs at all the sites were repeated every 15 min. The reference spectra are recorded at EL of 70° instead of 90° to avoid saturation of intensity. Because all the ELs were considered in the box air mass factor (A_{box}) calculation to retrieve the vertical profile, the choice of reference EL (70˚ or 90˚) is not an important issue for this study. The off-axis ELs are limited to < 10° to reduce the systematic error in the in-oxygen collision complex (O_4) fitting results (Irie et al., 2015), thereby maintaining high sensitivity in the lowest layer of the retrieved aerosol and trace gas profiles. Daily wavelength calibration using the high-resolution solar spectrum from Kurucz et al. (1984) is performed to account for the spectrometer's long-term degradation. The spectral resolution (full width half maximum: FWHM) is about 0.4 nm at 357 and 476 nm. The concentrations and profiles of aerosol and trace gases are retrieved using the Japanese vertical profile retrieval algorithm (JM2 ver. 2) (Irie et al., 2011, 2015). The algorithm works in three steps: (1) DOAS fittings, (2) profile/column retrieval of aerosol, and (3) profile/column retrieval of trace gases. Irie et al. (2008a, 2008b, 2011, 2015) described the retrieval procedures, and the error estimates. Herein we provide a short overview.

First, the differential slant column density (ΔSCD) of trace gases is retrieved using the DOAS technique (Platt 1994), which uses the nonlinear least-squares spectral fitting method, according to the following equation :

$$lnI(\lambda) = ln(I_o(\lambda) - c(\lambda)) - \sum_{i}^{n} \sigma_i(\lambda)\Delta SCD_i - p(\lambda) \qquad (1)$$

Therein, $I_o(\lambda)$ represents the reference spectrum measured at time t. $I_o(\lambda)$ is derived by interpolating two reference spectra (i.e., EL=70°) within 15 min before and after the complete sequential scan of the off-axis ELs at time t. ΔSCD represents the difference between the slant column density along the off-axis and reference spectrum. Second- and third-order polynomials are fitted to account, respectively, the wavelength-dependent offset $c(\lambda)$ and the effect of molecular and particle scattering $p(\lambda)$. In addition, $c(\lambda)$ accounts for the influence of stray light. The HCHO ΔSCD and NO_2 ΔSCD are retrieved respectively, from the fitting windows of 340–370 and 460–490 nm. Significant O_4 absorptions in the 338–370 and 460–490 nm fitting windows are used to retrieve the O_4 $\Delta SCDs$. The absorption cross-section data sources and the fitted absorbers in the HCHO and NO_2 fitting windows are given in Table 1. Figure 2 presents an example of the fitting results. O_4 fittings in both retrieval windows are shown in Fig S1 (supplementary information).
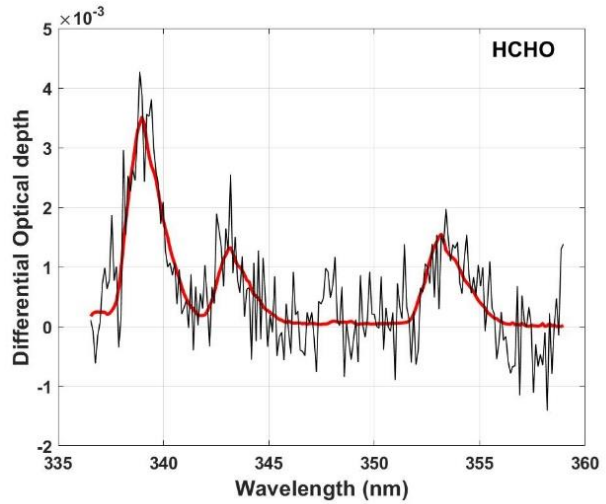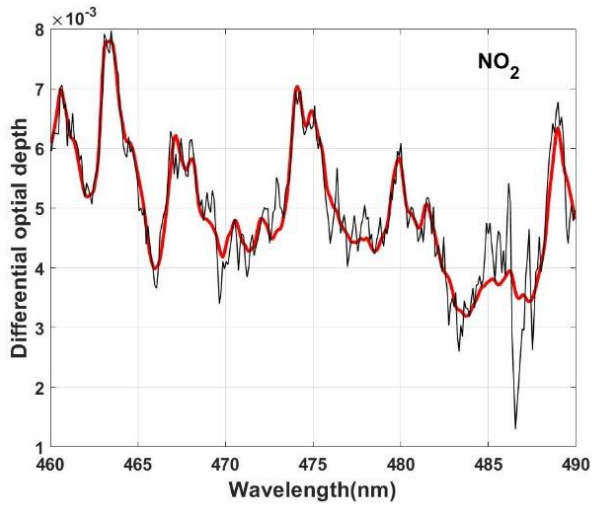
188 **Figure 2:** Examples of spectral fitting of NO₂ and HCHO, where red and black lines respectively show the scaled
189 cross-section and the summation of scaled cross-sections and fitting residuals. The example shows the
190 measurements of 10 April 2017, in Phimai at 10:00 LT at an EL of 2°.

191 In the second step, the aerosol optical depth (AOD) τ and the vertical profiles of the aerosol extinction
192 coefficient (AEC) k are retrieved using the approach developed by Irie et al, (2008a) which is based on
193 the optimal estimation method (Rogers, 2000). In this approach, the measurement vector y (representing
194 the quantities to be fitted) and state vector (representing the retrieved quantities) is defined as

195

196 $$y = (O_4 \Delta SCD(\Omega_1) \ldots \ldots \ldots \Delta SCD(\Omega_n))^T \qquad (2) \text{ and}$$

197 $$x = (\tau F_1 F_2 F_3)^T \qquad (3),$$

198

Table 1. Cross-section data references and absorbers fitted in the HCHO and NO_2 windows

Cross-section	Absorbers fitted	Data Source
O_3		Bougmil et al. (2003), 223K
NO_2	O_3, NO_2, H_2O, O_4, Ring	Vandaele et al. (1996), 295K
BrO		Fleischmann et al. (2004), 223K
Ring		Chance and Spurr (1997)
H_2O		Vandaele et al. (2005), 280K
O_4		Hermans et al. (2003), 296K
HCHO	O_3, NO_2, HCHO, BrO, O_4, Ring	Meller and Moortgart (2000), 293k

201

202

where n stands for the number of measurements within one complete scan of an EL sequence. Also, Ω
denotes the viewing geometry and includes three components: solar zenith angle (SZA), EL, and relative
azimuth angle (RAA). The F values determine the profile shape, with values between 0 and 1. The partial
AOD for 0–1, 1–2, 2–3, and above 3 km layers were defined respectively as AOD $\cdot F_1$, AOD $\cdot (1-F_1) F_2$,
and AOD $\cdot (1-F_1) (1-F_2) F_3$, and AOD $\cdot (1-F_1) (1-F_2) (1-F_3)$. The AEC profile from 3 to 100 km is derived

208 assuming a fixed value at 100 km and exponential AEC profile shape with a scaling height of ~1.6 km.

209 The k value at 100 km was estimated from Stratospheric Aerosol and Gas Experiment III (SAGE III)

210 aerosol data (λ=448 and 521 nm) taken at altitudes of 15–40 km. The negligible influence of such

211 assumptions on the retrievals in the lower troposphere has been demonstrated in sensitivity studies

212 reported by Irie et al (2012). Similarly, the AEC profiles at 2–3, 1–2, and 0–1 km were derived. Such

213 parameterization provides the advantage that the AEC profile can be retrieved using only the apriori

214 knowledge of the F values (profile shape) and little or no information related to the absolute AEC values

215 in the troposphere. Irie et al. (2008a) demonstrated that the relative variability of the profile shape, in

216 terms of 1-km averages, is smaller than that of the absolute AEC values. AEC profile shapes

217 corresponding to different F values is shown in Fig.S2 (supplementary information). However, the

218 vertical resolution and the measurement sensitivity cannot be derived directly with such a

219 parameterization (Irie et al., 2008a; 2009). The retrievals and simulations conducted by other groups for

220 similar geometries (i.e., Frieß et al., 2006) are used to overcome such limitations. The apriori values used

221 for this study were similar to those reported by Irie et al. (2011): AOD $= 0.21 \pm 3.0$, $F_1 = 0.60 \pm 0.05$, F_2

222 $= 0.80 \pm 0.03$, and $F_3 = 0.80 \pm 0.03$.

223 Then, a lookup table (LUT) of the box air mass factor (A_{box}) vertical profile at 357 and 476 nm is

224 constructed using the radiative transfer model JACOSPAR (Irie et al., 2015), which is based on the Monte

225 Carlo Atmospheric Radiative Transfer Simulator (MCARaTS) (Iwabuchi, 2006). The values of the single-

226 scattering albedo (s), asymmetry parameter (g), and surface albedo were, respectively, 0.95, 0.65 (under

227 the Henyey-Greenstein approximation), and 0.10. The U.S. standard atmosphere temperature and pressure

228 profiles were used for radiative transfer calculations. Uncertainty of less than 8% related to the usage of

229 fixed values of s, g, and a were estimated from sensitivity studies (i.e., Irie et al 2012). Results obtained

230 from JACOSPAR are validated in the study reported by Wagner et al. (2007). The optimal aerosol load

231 and the A_{box} profiles are derived using the A_{box} LUT and the O_4 ΔSCD at all ELs.

232 In the third step, the A_{box} profiles, HCHO and NO_2 ΔSCDs, and the nonlinear iterative inversion

233 method are used to retrieve the HCHO and NO_2 vertical column densities (VCDs) and profiles. Here the

234 NO_2 retrieval is explained.

235

236   For trace gas retrieval, the measurement vector and state vector are defined as

237
$$y = (NO2\Delta SCD(\Omega_1) \dots \dots \dots NO2\Delta SCD(\Omega_n))^T \qquad (4) \text{ and}$$

238

239
$$x = (VCD f_1 f_2 f_3)^T \qquad (5)$$

240   VCD represents the vertical column density below 5 km. The f values are the profile shape factors.

241 Above the 5 km layer, fixed profiles are assumed. Similarly, to aerosol retrieval, the partial VCD values

242 for the 0–1, 1–2, 2–3, and 3–5 km is defined respectively as VCD $\cdot f_1$, VCD $\cdot (1-f_1) f_2$, VCD $\cdot (1-f_1) (1-f_2)$

243 f_3, and VCD $\cdot (1-f_1) (1-f_2) (1-f_3)$. Finally, the volume mixing ratio (VMR) is calculated using the partial

244 VCD, and U.S. standard atmosphere temperature and pressure data scaled to the respective surface

245 measurements.

246   The calculated vertical profile is converted to NO_2 $\Delta SCDs$ using the A_{box} LUT constructed for aerosol

247 retrieval. However, the trace gas wavelengths differed from the representative wavelengths of A_{box} LUT

248 (357 and 476 nm). Therefore, the AOD at the trace gas wavelength is estimated, converting the retrieved

249 AOD to the closer aerosol wavelength of 357 or 476 nm, assuming the Angstrom exponent value of 1.00.

250 The choice of the Angstrom exponent value can induce uncertainty in the retrieved VCDs. However, such

251 uncertainty was found to be non-significant compared to that of A_{box} profiles. Uncertainty in the A_{box}

252 profiles are assumed to as high as 30 to 50%. Such values are derived empirically from comparison with

253 sky radiometer and LIDAR observations (i.e., Irie et al., 2008b). Then, the A_{box} profiles from the LUT

254 corresponding to the recalculated AOD values are selected. The dependence of the A_{box} profiles on the

255 concentration profiles is expected to be low because both HCHO and NO_2 are optically thin absorbers

256 (Wagner et al., 2007; Irie et al., 2011). For every 15 min (time necessary for one complete scan of ELs),

257 20% (the mean ratio of the retrieved VCD to maximum ΔSCD) of the maximum trace gas $\Delta SCDs$ is used

258 as a priori information for the VCD retrievals. The a priori error is set to 100% of the maximum trace gas

259 ΔSCD. Figure 3 presents the mean averaging kernel (AK) of the HCHO and NO_2 retrievals during the dry

260 season at Phimai. The area (Rodgers, 2000) provides an estimate of the measurement contribution to the

261 retrieval. The total area is the sum of all the elements in the AK and weighted by the a priori error (Irie et

262 al. 2008a). The areas for VCD and $f1$ of NO_2 retrieval are 1 and 0.6, respectively. The $f2$ and $f3$ values

263 are much smaller. Consequently, at first, the a priori profiles were scaled, and later f values determined

264 the profile shape. The VCD area is close to unity, and therefore, the retrieved VCD is independent of the
265 a priori values. Irie et al (2008) conducted sensitivity studies of choice of the f values and reported
266 negligible effect on the retrievals.

267
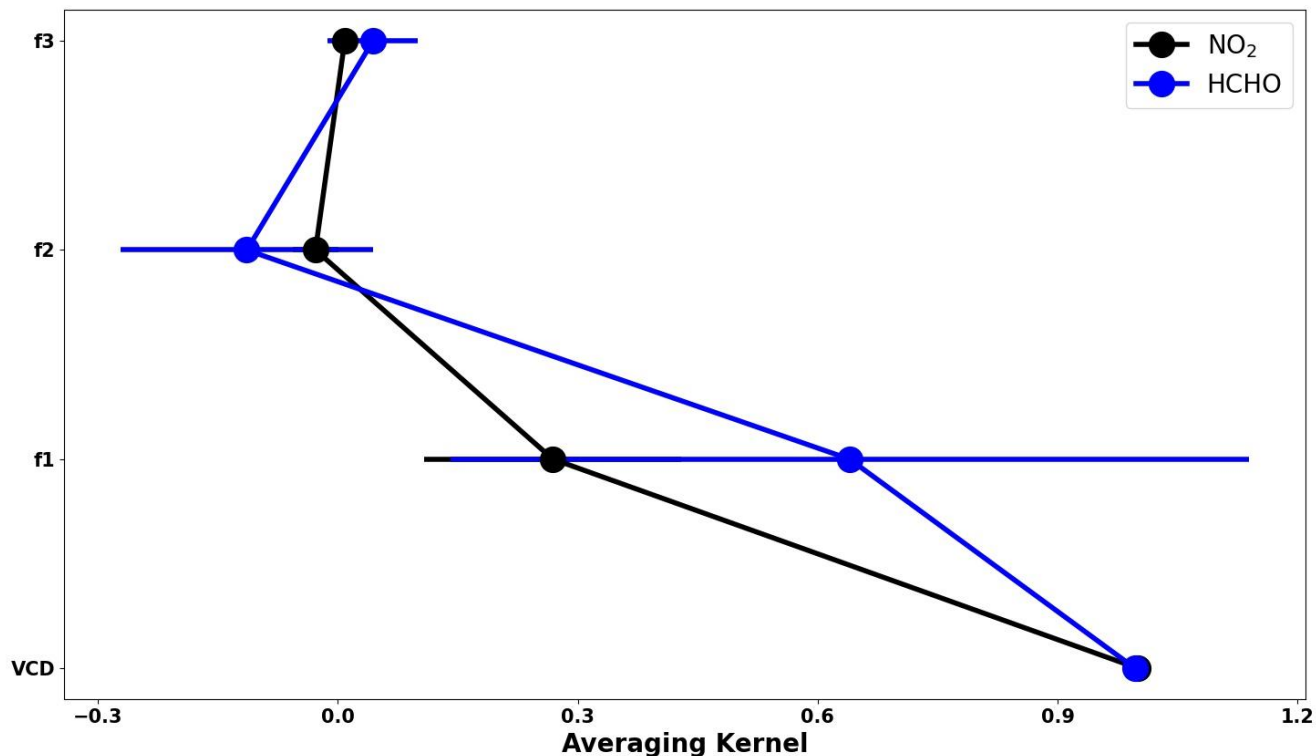
268

269 **Figure 3:** Mean averaging kernel of the NO$_2$ and HCHO retrievals from observations at Phimai during 2017. The
270 error bars represent the 1-sigma standard deviation of the mean values.

271

272   The total error of the retrieval consists of random and systematic errors. The measurement error
273 covariance matrix constructed from the residuals of the respective trace gas ΔSCDs is used to estimate
274 the random error. The systematic error is calculated while assuming uncertainties as high as 30 and 50%
275 in the retrieved AOD (or the corresponding A_{box} values). Table 2 shows the total estimated error. Aside
276 from the random and systematic error, more sources of error might exist. For instance, the bias in the ELs

277 can induce uncertainties in the retrieved products. However, Hoque et al. (2018) demonstrated that such

278 biases had a non-significant effect on the final retrieved products, mostly less than 5%.

279   The cloud screening procedure is similar to that described by Irie et al. (2011) and by Hoque et al.

280 (2018a, 2018b). During the retrieval steps, retrieved AOD values greater than 3 are excluded, because

281 optically thick clouds are primarily responsible for such large optical depth. Filtering based on the

282 residuals of O_4 and the trace gas ΔSCDs is also used to screen clouds. Larger residuals likely occur due

283 to two reasons: (1) when the constructed profile is too simple to represent the true profile, particularly

284 with a steep vertical gradient of extinction due to clouds, and (2) rapid changes in optical depth within 30

285 min (time for one complete scan) (Irie et al, 2011).The screening criteria are: respective residuals of O_4,

286 HCHO, and NO_2 ΔSCDs < 10%, < 50%, and <20%, and the degrees of freedom of retrievals greater than

287 1.02. The threshold values were determined statistically corresponding to the mode plus one sigma (1σ)

288 in the logarithmic histogram of relative residuals.

289

290 **Table 2.** Estimated Errors (%) for the NO_2 and HCHO concentration in 0-1 km layer, retrieved using the

291 JM2 algorithm

Retrieved Product	Random error	Systematic error	Error related to instrumentation	Total error
NO₂	10	12	5	16
HCHO	16	25	5	30

292

293

294 ## 2.3 CHASER simulations

295 CHASER 4.0 (Version 4) (Sudo et al., 2002; Sudo and Akimoto, 2007; Sekiya and Sudo, 2014), coupled

296 online with the MIROC-AGCM atmospheric general circulation model (AGCM) (K-1 model developers,

297 2004) and the SPRINTARS aerosol transport model (Takemura et al., 2005, 2009), is a global chemistry

298 transport model used to study the atmospheric environment and radiative forcing. In addition, several

299 updates, including the introduction of aerosol species (sulfate, nitrate, etc.) and related chemistry,
300 radiation, and cloud processes, have been implemented in the latest version of CHASER.

301   CHASER can calculate the concentrations of 92 species through 263 chemical reactions (gaseous,
302 aqueous, and heterogeneous chemical reactions) considering the chemical cycle of O_3–HO_x – NO_x –CH_4–
303 CO along with oxidation of non-methane volatile organic compounds (NMVOCs)(Miyazaki et al., 2017).
304 The chemical mechanism is largely based on the master chemical mechanism (MCM,
305 http://mcm.york.ac.uk)(Jenkin et al., 2015). CHASER simulates the stratospheric O_3 chemistry
306 considering the Chapman mechanisms, catalytic reactions related to halogen oxides (HO_x, NO_x, ClO_x,
307 and BrO_x), and polar stratospheric clouds (PSCs). Resistance-based parameterization (Wesely, 1989),
308 cumulus convection, and large-scale condensation parameterizations are used to calculate dry and wet
309 depositions. The piecewise parabolic method (Colella and Woodward, 1984)

310

311 **Table 3:** Settings of the CHASER simulations used in this study

Simulation	Anthropogenic emissions	Pyrogenic emissions	Biogenic emissions	Soil NO_x emission	Other physical and chemical processes
Standard	ON	ON	ON	ON	ON
L1_HCHO	ON	Pyrogenic VOCs switched	ON	ON	ON
L1_opt	ON	OFF	Reduced by 50%	ON	ON
L1_NO₂	ON	ON	ON	OFF	ON

| L2 | Anthropogenic VOC emissions switched OFF | ON | ON | ON | ON |

and the flux-form semi-Lagrangian schemes (Lin and Rood, 1996) calculate advective tracer transport. CHASER simulates tracer transport on a sub-grid scale in the framework of the prognostic Arakawa–Schubert cumulus convection scheme (Emori et al., 2001) and the vertical diffusion scheme (Mellor and Yamada, 1974). In this study, CHASER simulations were conducted at a horizontal resolution of $2.8° \times 2.8°$, with 36 vertical layers from the surface to ~50 km altitude and a typical time step of 20 min. The meteorological fields simulated by MIROC-AGCM were nudged toward the six-hourly NCEP FNL reanalysis data at every model time step.

The anthropogenic, biomass burning, lightning, and soil emissions of NO_x were incorporated into CHASER simulations. Anthropogenic emissions were based on HTAP_v2.2 for 2008. Biomass burning and soil emissions from the ECMWF/MAC (Global Fire Assimilation System (GFAS)) reanalysis were used. The biogenic emissions for VOCs are based on the process-based biogeochemical model the Vegetation Integrative SImulator for Trace gases (VISIT) (Ito and Inatomi, 2012) simulations. The NO_x production from lightning is calculated based on the parameterization of Price and Rind (1992) linked to the convection scheme of the AGCM (Sudo et al., 2002). Isoprene, terpene, acetone, and ONMV emissions estimates in the VISIT inventory during July were 2.14×10^{-11}, 4.43×10^{-12}, 1.60×10^{-12}, and 9.93×10^{-13} $kgCm^{-2}s^{-1}$. Global NO_x emissions of 43.80 $TgNyr^{-1}$ are used in the simulations, considering industries (23.10 $TgNyr^{-1}$), biomass burning (9.65 $TgNyr^{-1}$), soil (5.50 $TgNyr^{-1}$), lightning (5 $TgNyr^{-1}$), and aircrafts (0.55 $TgNyr^{-1}$) as significant sources. Global isoprene emissions from vegetation were set to 400 $TgCyr^{-1}$.

NO$_x$ emissions in India were estimated as 14 Tg/yr in 2016, almost two-fold increase since 2005 (~8 Tg/yr), with the energy and transportation sector being the largest contributor (Sadavarte et al 2014). Indian anthropogenic non-methane VOCs (NMVOCs) emissions in 2010 were estimated ~ 10 Tg/yr , with respective contributions of 60, 16, and 12% from residential, solvents, and the transport sector(Sharma et al 2015). In Japan, vehicular exhausts (14 - 25%), gasoline vapor (9 - 16%), liquefied natural gas (7 - 10%), and liquefied petroleum gas (49 - 71%) contribute to the total VOC concentrations (Morino et al., 2011), with annual NMVOC emission of ~2 Tg (Kannari et al., 2007). Annual NO$_x$ emissions in Japan and Thailand in 2000 was estimated as ~2000 and 591 kt/yr, with the largest contribution from transport-oil use, followed by the energy and industrial sector (Ohara et al., 2007). Annual anthropogenic VOC emissions in Thailand are approximately   0.9 Tg, with 43, 38, and 20% contributed, respectively, from industrial, residential and transportation sectors (Woo et al; 2020).

Multiple CHASER simulations with different settings used for sensitivity studies are presented in Table 3.

2.4 Satellite observations

Tropospheric NO$_2$ and HCHO retrievals from the Ozone monitoring Instrument (OMI) were also used to evaluate the model simulations. The ultra-violet nadir-viewing spectrometer OMI, on board the Aura satellite measures backscattering solar radiation covering the spectral range of 270 – 500 nm (Levelt et al., 2006). In an ascending sun-synchronous polar-orbit, OMI crosses the equator at 13:40 LT (local time (Zara et al., 2018). OMI measures at a spatial resolution of 13×24 km^2 and provides daily global coverage of various trace gases including NO$_2$ and HCHO. The NO$_2$ and HCHO datasets were obtained respectively from the TEMIS (www.temis.nl, last accessed on 2022/04/23) and aeronomie (https://h2co.aeronomie.be/, last accessed 2022/05/03) websites. NO$_2$ tropospheric columns retrieved using the DOMINO version 2.0 (Boersma et al., 2011) algorithm were used for the analysis. Data meeting the following criteria were selected: cloud fraction < 0.5, SZA < 70˚, surface albedo < 0.3, quality flags =0, and cross-track quality flags= 0. For HCHO, we used the BIRA-IASB v14 (De Smedt et al 2015)

358 retrieved products. The data filtering criteria was the following: cloud fraction < 0.4, SZA<70˚, AMF >
359 0.2, quality flag=0, and cross-track quality flag =0.

360

361

3 Results and discussion

3.1 Results from MAX-DOAS observations

3.1.1 HCHO seasonal variation

365 The monthly mean HCHO mixing ratios in the 0–1 and 0–2 km layers from January 2017 – December
366 2018 and the corresponding one sigma (1σ) standard deviations indicating the variation ranges for the
367 three sites are presented in Fig. 4. The HCHO levels at the Phimai site show a consistent seasonal cycle,
368 characterized by high VMRs during the dry season. Such enhancement is related to the influence of
369 biomass burning during the dry season, which has been well documented in the work of Hoque et al.
370 (2018). The HCHO mixing ratio at Phimai reach a peak in March or April, with a maximum of 4 – 6
371 ppbv. The variation in the peak concentration and timing depends mainly on the intensity of biomass
372 burning activities. During the wet season, the HCHO concentrations are mostly within 2–3 ppbv,
373 indicating a two-fold increase in HCHO abundances during the dry season. The daily mean HCHO
374 amounts (0 –1 km) are 0.78 - 9.84 ppbv, representing seasonal modulation of 134%.
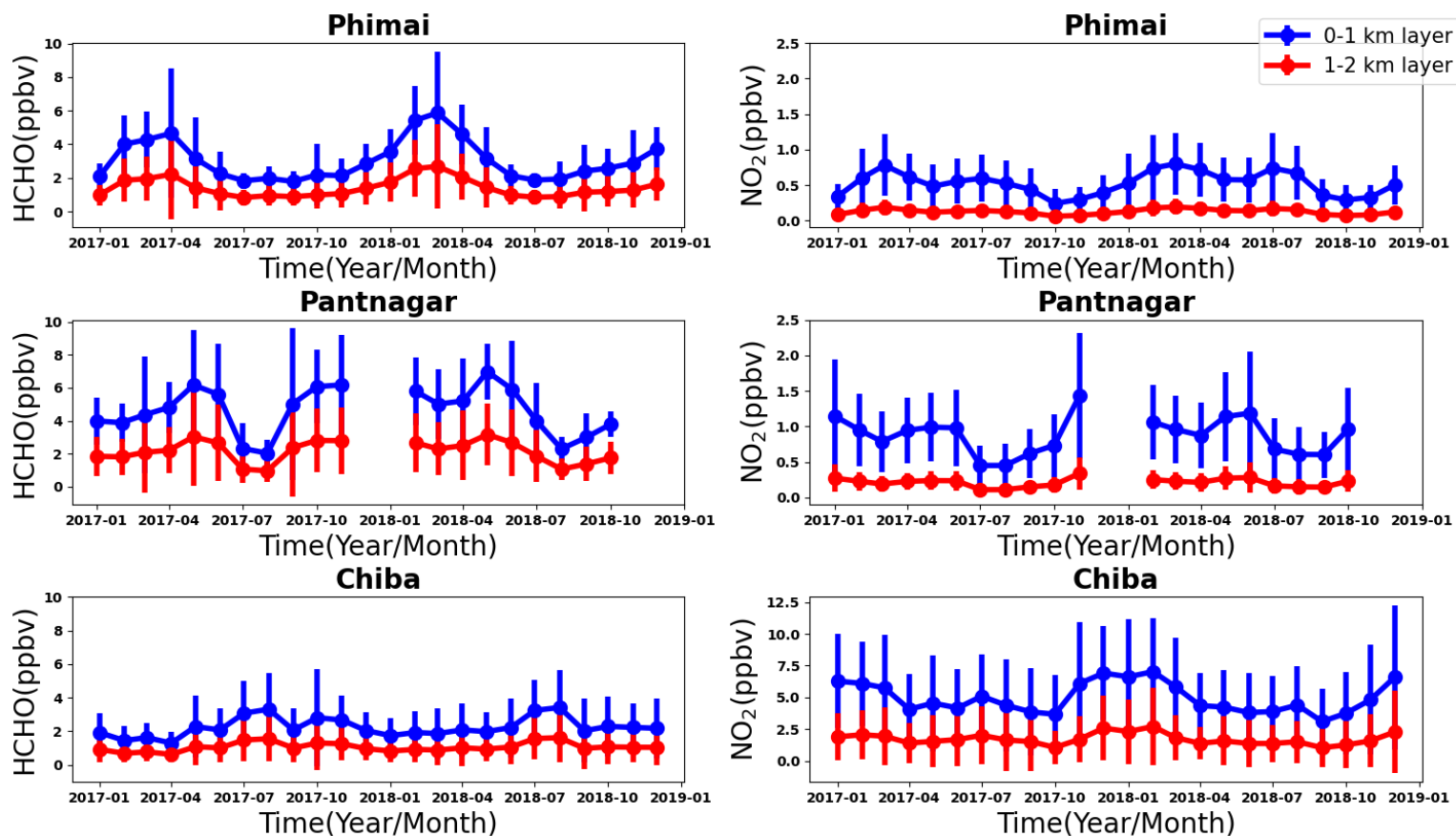
Figure 4: Seasonal variations in the HCHO (left panel) and NO$_2$ (right panel) mixing ratios in the 0 - 1 (blue) and 1 - 2 (red) km layers at Phimai, Pantnagar, and Chiba. The error bars represent the one sigma standard deviation of the mean values. The gaps in the plots for the Pantnagar site indicate the unavailability of observations during the investigated period.

Seasonal variation of HCHO in the 0–1 km layer at the Pantnagar site has been elucidated by Hoque et al. (2018b). Here, the results are replotted to verify the consistency of the seasonal variations. Observations made during autumn 2018 were not available because of problem with the spectrometer. Consistent seasonal variation of HCHO abundances is observed at the Pantnagar site, with enhanced concentrations during the spring. The Pantnagar site is affected by biomass burning during spring and autumn (Hoque et al., 2018b), explaining the high mixing ratios found during spring. In both years, the

388 maximum HCHO mixing ratios are ~6 ppbv. The springtime peak occurred in May. The HCHO
389 concentrations during the monsoon are ~35% lower than in the spring, indicating a strong effect of the
390 monsoon on the HCHO concentrations found for Pantnagar. The seasonal modulation of HCHO at
391 Pantnagar estimated from the daily mean concentrations is 107%. The peak HCHO mixing ratio at
392 Pantnagar is almost twice that of in Pune city (~ 3 ppbv) (Biswas and Mahajan, 2021), a site in the IGP
393 region. The HCHO seasonality at the two sites are found to be dissimilar, because of differences in the
394 VOC sources, however, lower mixing ratios during the monsoon is consistent. From another site in the
395 IGP region (i.e., Mohali), Kumar et al., (2020) reported lowest HCHO VCDs during March 2014 and
396 2015, attributing them to lower biogenic and anthropogenic VOC emissions. At Pantnagar, the lowest
397 HCHO mixing ratios are observed during the monsoon. The rainfall events in the IGP region shows strong
398 annual variability (Fukushima et al. 2019). Discrepancies between the sites might be related to the rainfall
399 pattern.

400 Under the influence of biomass burning, the maximum monthly HCHO mixing ratios at Phimai and
401 Pantnagar are similar (~6 ppb). The maximum instantaneous HCHO VMR during biomass burning
402 influence in Phimai and Pantnagar are, respectively, 26 and 30 ppbv. Zarzana et al. (2017) reported HCHO
403 abundances of ~60 ppbv in fresh biomass plumes in the US. The lower values obtained from our
404 measurements might be attributable to (1) more aged plumes intercepted by the MAX-DOAS instruments
405 and (2) differences in the types of biomass fuel used. Comparison to reports of literature indicates that the
406 retrieval of HCHO under biomass burning is reasonable.

407 The summertime maximum and wintertime minimum characterize the seasonal variations of HCHO at
408 the Chiba site, with a peak at ~3 ppbv. The HCHO concentrations are ~2 ppbv during other seasons,
409 which are similar to the HCHO concentrations in Phimai during the wet season. The seasonal variation
410 amplitudes of HCHO at Chiba is ~94%. For a site with similar seasonal variation (i.e., summertime
411 maximum and wintertime minimum), Franco et al. (2015) reported HCHO seasonal modulation of 88%.

412 The HCHO VMRs in the 1–2 km layers at all three sites are lower, almost 50% the value of the
413 concentrations in the 0–1 km layer. The HCHO seasonal variation amplitudes at Phimai, Pantnagar, and
414 Chiba sites are, respectively, 131%, 102%, and 90% when calculated based on the HCHO concentration
415 in the 1–2 km layers. The modulation was even lower when retrieved values for the 2–3 km layer is used.

3.1.2 NO$_2$ seasonal variation at the three sites

Figure 4 also shows the seasonal variation of NO$_2$ in the 0–1 and 1–2 km layers at the three sites. The error bars represent the 1σ standard deviation of the mean values. The NO$_2$ seasonal variations at Phimai and Pantnagar sites are similar to those of HCHO. Pronounced peaks attributable to biomass burning influence is observed during the dry season at Phimai (~0.8 ppbv) and during spring (1.2 ppbv), and post-monsoon (1.4 ppbv) at Pantnagar. The lowest NO$_2$ mixing ratios at Phimai and Pantnagar are, respectively, ~0.2 and 0.5 ppbv. The NO$_2$ VMRs at Chiba is higher (~7 ppbv) during winter. The longer lifetime of NO$_x$ and lower NO/NO$_2$ ratio because of lower photochemical activity in winter lead to high NO$_2$ mixing ratios at Chiba (Irie et al., 2021).

At Phimai, the NO$_2$ mixing ratios in both seasons are similar. However, when Hoque et al. (2018a) reported the seasonal variations in NO$_2$ at Phimai during 2015 – 2018, the dry season mixing ratios were higher. Table 4 shows the number of fire events during the dry seasons during 2015 - 2018. The fire data are extracted from the MODIS Active Fire Detections database (https://firms.modaps.eosdis.nasa.gov, last accessed on 2021/12/15). Data fulfilling the following criteria were chosen – (a) data points located within 100 km of the Phimai site, (b) confidence of the data greater than 70%, and (c) observations during the daytime. The lower fire counts during 2017 - 2018 compared to those of 2015 - 2016 period coincide with the lower NO$_2$ levels in the former. Fire counts varied between 2017 and 2018 but did not affect the NO$_2$ levels. However, HCHO levels changed with the number of fire occurrences between 2015 – 2018 (i.e., Figure 4 and Hoque et al.,2018a).

At such low NO$_2$ levels at Phimai, soil NO$_x$ emissions are likely to make a greater contribution to NO$_2$. Although NO$_2$ is not emitted directly from soils, biological processes emit NO, which is rapidly converted to NO$_2$ (Hall et al., 1996). In addition, many studies have established a relation between soil moisture and NO emissions (Carden et al., 1993; Zheng et al., 2000; Schindlbacher et al., 2004; Huber et al., 2020). The potential contribution of soil NO$_x$ emissions, as inferred from CHASER simulations, is discussed in section 3.4.2.

Table 4: Number of fire events occurring during the dry season (January - April) at Phimai from 2015 - 2018. Selection criteria of the data are the following: (1) situated within 100 km of the site, (2) confidence level > 70%, and (c) daytime measurements.

Dry season years	Number of fire events
2015	84
2016	98
2017	62
2018	77

444

445

3.1.3.1 The HCHO to NO₂ ratio (R_{FN}):

447 The HCHO to NO_2 (R_{FN}) ratio is regarded as an indicator of high ozone O_3 sensitivity (Martin et al., 2004;

448 Duncan et al., 2010). The O_3 production regime is characterized as VOC-limited for $R_{FN} < 1$ and NO_x-

449 limited when $R_{FN} > 2$, and the values in the range 1-2 are said to be in the transition/ambiguous region

450 (Duncan et al., 2010; Ryan et al., 2020). Subsequent to a report of Tonnesen and Dennis (2000), several

451 studies used R_{FN} estimated from satellite and ground-based observations to infer O_3 sensitivity to NO_x

452 and VOCs (Martian et al., 2004; Duncan et al., 2010; Jin and Holloway et al.,2015; Mahajan et al., 2015;

453 Irie et al.,2021; etc.). However, the effectiveness of R_{FN} is still under discussion primarily based on two-

454 points- (1) the range of the transition region to categorize the VOC and NO_x -limited region, and (2) the

455 altitude dependence of R_{FN} (Jin et al., 2017). Most of the studies described above used the transition range

456 ($1 < R_{FN} < 2$) proposed by Duncan et al. (2010). Schroeder et al. (2017) reported that a common transition

457 (i.e., $1 < R_{FN} < 2$) range might not be valid globally. Instead, it should be calculated based on the region.

458 First, the results based on the standard transition range are discussed herein, and then its applicability to

459 the study regions is assessed.

460 Figure 5 shows scatter plots of the daily mean NO_2 and HCHO concentrations in the 0 - 2 km layer at the

461 three sites, color-coded with the respective O_3 concentrations (0-2 km). Retrieval of the JM2 O_3 product

462 is explained by Irie et al. (2011). The O_3 concentrations for SZA $< 50°$ are used to minimize stratospheric

463 effects. This criterion on the SZA is also applied for the selection of the NO_2 and HCHO concentrations.

464 Although not checked here, the JM2 O_3 product showed good agreement with ozonesonde measurements

465 in Tsukuba (Irie et al., 2021). Most of the high O_3 occurrences fall in the $R_{FN} > 2$ region at Phimai and

466 Pantnagar and in $R_{FN} < 1$ at Chiba. The common transition range classifies the O_3 production regime as

467   NO_x-limited at Phimai and Pantnagar and VOC-limited at Chiba. At all sites, the R_{FN} values tend to be

468   biased to a particular regime (i.e., NO_X - or VOC-limited), with only 4 and 2% of the ratios in the range

469   0 - 2, at Phimai and Pantnagar, respectively. This finding suggests that the transition occurs at a higher or

470   lower ratio than the common definition. Recent report by Souri et al. (2020) found that the NO_2-HCHO

471   relation plays an important role in determining the transition region and derived a formulation from

472   accounting for the NO_2-HCHO chemical feedback in the ratios as

$$HCHO = m * (NO_2 - b) \qquad (6)$$

474   where m and b respectively denote the slope and intercept. Equation (6) is based on observations, which

475   means that the regionally adjusted fitting coefficients will reflect the local NO_2 - HCHO relation. Solving

476   equation (6), the transition line estimated from the observations in the 0 - 2 km layer, is shown in Fig 5

477   (bottom panel). Rather than a range, the method calculates a single transition line, which corresponds to

478   the NO_2 - HCHO feedback. The regions above and below the transition line are characterized, respectively

479   as VOC- and NO_x -limited or other.

480
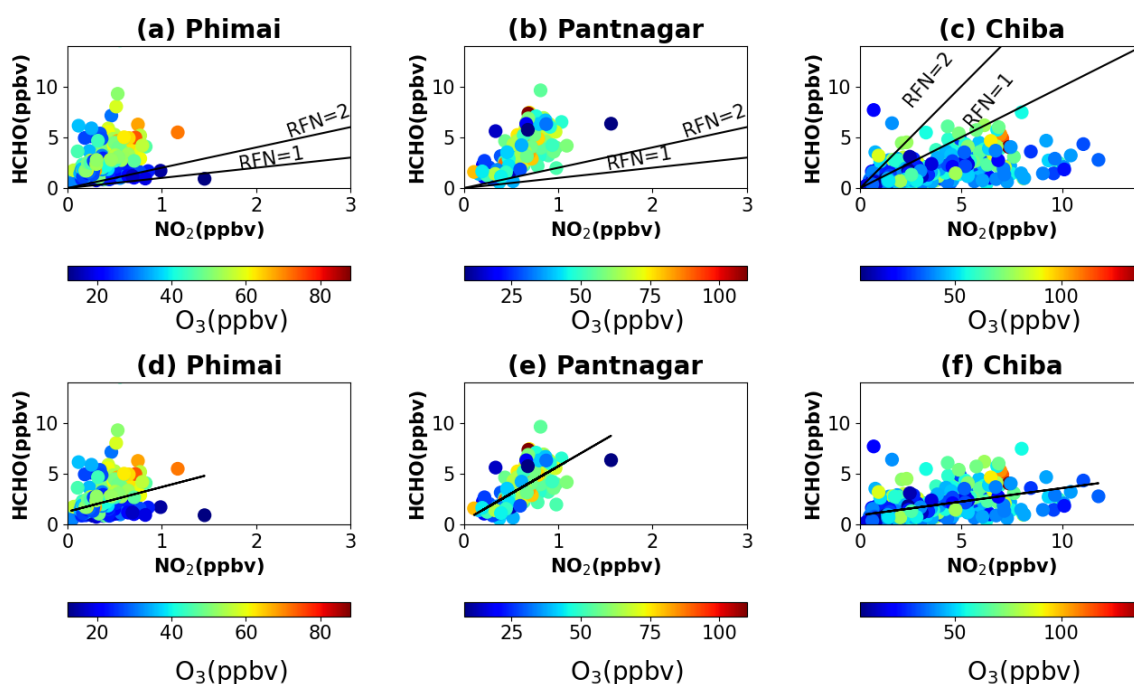
Figure 5. Scatter plots of HCHO and NO_2 concentrations in the 0-2 km layer at (a, d) Phimai, (b, e) Pantnagar, and (c, f) Chiba, coloured with the O_3 concentrations in the 0-2 km layer at the respective sites. The solid lines in the top panel represent $R_{FN} = 2$ and $R_{FN} = 1$ benchmarks. The black lines in the bottom panel are calculated according to equation (1).

The revised transition line at Phimai and Pantnagar is apparently more reasonable than the earlier method. At Phimai, the transition line almost clearly distinguishes between the high and low O_3 occurrences. It is perceptible that when the HCHO concentrations are higher than NO_2, the transition of the regimes is likely to occur at higher R_{FN} values. The minimum and mean R_{FN} value along the transition line are 3.62 and 6.78, respectively. Because Phimai is a VOC-rich environment, the regime transition occurs at higher R_{FN} values than by the conventional definition. This finding echoes the results reported by Schroeder et al. (2017) for a regionally variable transition region. The definition of $R_{FN} < 1$ as a VOC -limited regime might not be valid in this case. Considering the mean R_{FN} ratio along the transition line (i.e., 6.78), the VOC- and NO_x -limited (and other) regimes are defined, respectively as $R_{FN} < 6.78$ and $R_{FN} > 6.78$. Based on this definition, around 34% (65%) of the ratios are higher (lower) than 6.78, classifying Phimai as a dominant VOC-limited region, which contradicts earlier results. Biomass burning affects Phimai during January - April and is a significant emission source in addition to biogenic emissions. Thus, high O_3 occurrences likely occur only 30% of the time during a year. Such events mostly lie above the transition line.

At Pantnagar, high O_3 occurrences lie below (42%) and above (57%) the transition line, indicating that O_3 production is sensitive to both HCHO and NO_2 which contradicts results reported by Biswas et al. (2019). Based on satellite and ground-based observations, the study estimated the R_{FN} values at a site in the IGP as > 4 and > 2 respectively, and regarded the O_3 regime as NO_x-limited. Mahajan et al. (2015) reported R_{FN} values of less than 1 over the IGP region signifying as a VOC-limited region. Pantnagar is a sub-urban site situated beside a busy road. Therefore, effects of anthropogenic emissions are expected year-round, especially with pyrogenic emissions during the spring and post-monsoon period. O_3 sensitivity to both NO_x and VOCs in the north-west IGP region has also been reported by Kumar and Sinha (2021). Therefore, the balance between the VOC and NO_x-limited region in the IGP is reasonable. The mean and minimum R_{FN} value along the transition line are, respectively, 5.59 and 6.09. The minimum

509 value (i.e., 5.59) is higher than Phimai (3.26), suggesting higher VOC levels at Pantnagar, consistent with
510 the observations.

511   At Chiba, 60% of the R_{FN} values lie below the transition line, suggesting a dominant VOC-limited
512 region, which is consistent with the results reported by Irie et al. (2021). The minimum and the mean R_{FN}
513 along the transition line are, respectively, 0.33 and 0.72. The transition occurs at a low R_{FN} value because
514 of higher NO_2 levels. The fact that, 40% of the R_{FN} values are above the transition region suggests a
515 moderate effect of HCHO on the O_3 sensitivity at Chiba.

516   Although the new classification results are apparently reasonable, they should be interpreted with
517 care. Our current understanding of R_{FN} contradicts the classification of rural sites as VOC-limited. Despite
518 the theoretical and observational evidence (i.e., Souri et al.,2020), the classification of regimes based on
519 a single transition line is not yet well-established. Schroder et al. (2017) used regionally varying transition
520 ranges. Moreover, (a) the number of observations and (b) the systematic and retrieval errors can affect
521 the estimations and classifications. These findings are expected to contribute to the ongoing discussion
522 about the effectiveness of R_{FN}. However, the results support the idea of a regionally varying transition
523 range.

524

525 **3.1.3.2 R_{FN} profiles**
526 Figure 6 shows the seasonal mean R_{FN} profiles at the three sites. Only the profiles during the high O_3
527 concentrations at the sites (i.e., March at Phimai, May at Pantnagar, and February at Chiba) are shown.
528 The R_{FN} values are likely increase with height because of the lower vertical gradient of NO_2, than that of
529 HCHO (Fig.4). It is particularly interesting that, the R_{FN} values are similar in the 1-2 km height under
530 biomass burning conditions, suggesting a small variation in the HCHO loss rate in the particular layer. At
531 both sites, the HCHO concentration at 1.5 km is about 3 ppbv. At Chiba, a considerable amount of NO_2
532 in the higher layers increases the ratio up to 2 km height. Beyond 2 km, the ratio variation at all sites is
533 opposite that found for the surface. The gradient issue of R_{FN} has been discussed explicitly by Jin et al.
534 (2017). They proposed a conversion factor to account for gradient differences in the surface and column-
535 derived R_{FN} values, estimating the conversion factor from the model simulated surface and column

536 abundances of NO₂ and HCHO. We adopt the method reported by Jin et al. (2017) for this study using
537 the CHASER simulated NO₂ and HCHO concentrations and vertical columns.

538 First, CHASER simulated near-surface NO₂ and HCHO concentrations were converted to number
539 density. The effective boundary layer height (E) (Halla et al., 2011; Jin et al., 2017) was estimated.

540

541 $$E_{NO_2} = \frac{NO_2\ total\ column}{NO_2\ near-surface\ number\ density} \qquad (7)$$

542

543 $$E_{HCHO} = \frac{HCHO\ total\ column}{HCHO\ near-surface\ number\ density} \qquad (8)$$

544 Therein, E_{NO_2} and E_{HCHO} respectively denote the effective boundary layer heights of NO₂ and HCHO.
545 In the second step, the column to surface conversion factor (F) was calculated according to the following
546 equation:

547 $$F = \frac{E_{HCHO}}{E_{NO_2}} \qquad (9)$$

548 The seasonal variation of F for the three A-SKY sites and the associated 1σ standard deviation of the
549 mean values are depicted in Fig. 7(c). The F values over East Asia reported by Jin et al. (2017) were ~2,
550 without marked seasonal variation. CHASER estimated F values over Chiba range between 1–2.5, which
551 is apparently reasonable, when compared with literature values. Values reported in literature for polluted
552 regions (NO₂ > 2.5 molecules cm⁻²) considered simulation data for 1–2 PM, but the estimates for this
553 study used daytime (07:00 – 18:00) simulations.
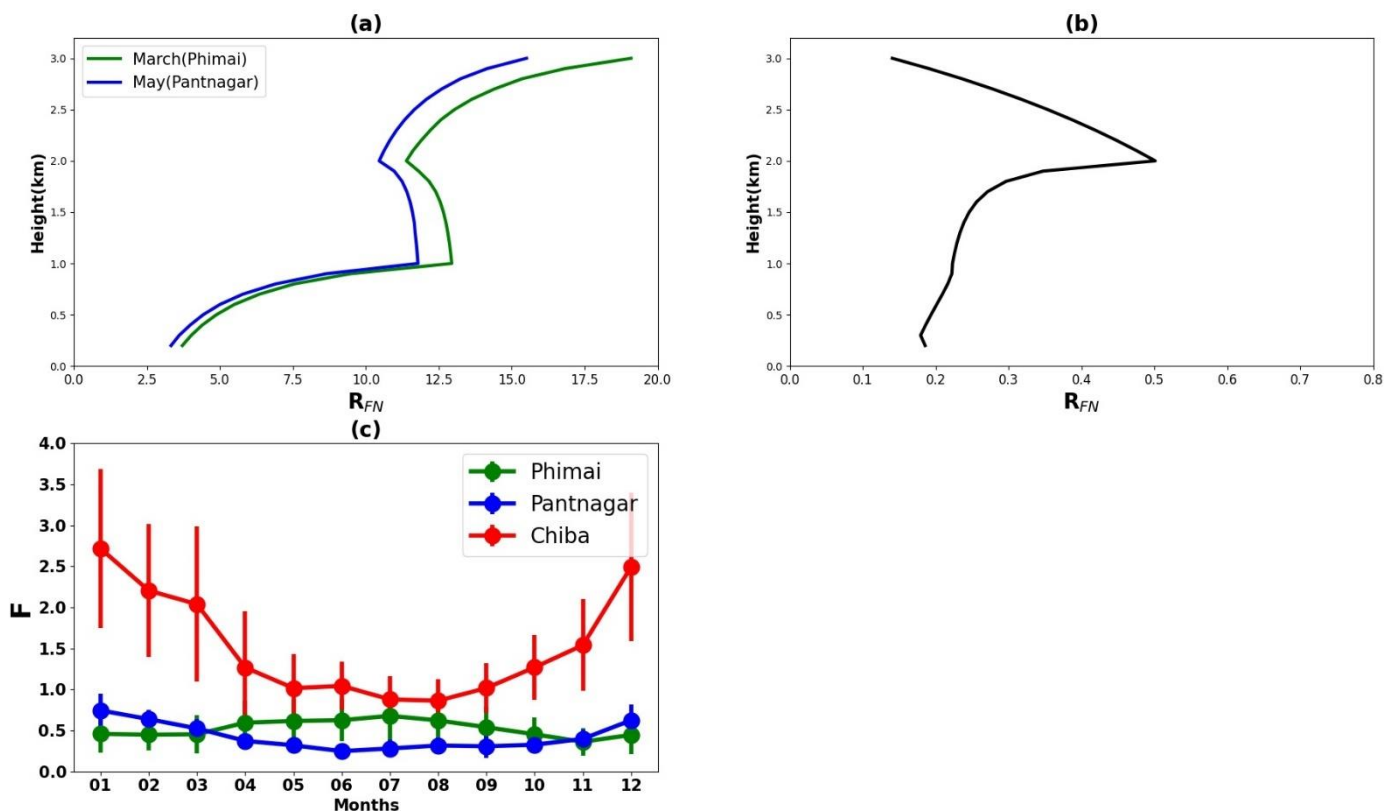
554

555 **Figure 6**: Seasonal mean R_{FN} profiles during (a) March and May at Phimai and Pantnagar, respectively, and (b)
556 February at Chiba. (c) Seasonal variations in the column to surface conversion factor (F) for the Phimai, Pantnagar,
557 and Chiba sites, estimated from the CHASER simulated HCHO and NO_2 surface concentrations and VCD. The
558 simulated data from 07:00 – 18:00 in 2017 were used to estimate the F values. The error bars represent the one
559 sigma standard deviation of the mean values.

560

561   The F values for Pantnagar are mostly less than 1, with no distinctive seasonal variation. Mahajan et
562 al. (2015) reported OMI-derived R_{FN} values < 1 over the IGP region. When this estimated conversion
563 factor is used with the values reported by Mahajan et al. (2015), the discrepancy in the satellite and
564 ground-based observation derived R_{FN} values in the IGP region are reduced indicating that the estimated
565 F values for the Pantnagar site can be representative for the IGP region. The F values at the Phimai site

566 range were 0.5–1. Our estimated F values for the Phimai and Pantnagar sites are useful as representative

567 values for these respective regions, which can be improved further based on the results.

568

3.2 Global Evaluation of the CHASER model

570 This section describes the evaluation of CHASER NO_2 and HCHO columns for 2017 against OMI

571 observations. The OMI AKs were applied to the CHASER outputs to account for the altitude-dependence

572 of the retrievals. First, 2-houly simulated profiles (NO_2 and HCHO) were sampled closest to the

573 observation time. Secondly, AKs were applied to the sampled profiles and the mean profile was

574 calculated. Thirdly, both the simulations and observations were averaged on a 2.8˚ bin grid. The month

575 of July and December were discarded from the NO_2 comparison because few coincident days (only five

576 days) were available after filtering. It should be noted that simulations based on old NO_x emission

577 inventory will likely affect the model-satellite comparison results. However, the current study has not

578 assessed such impact due to technical issues related to using an updated emission inventory. All these

579 issues will be addressed in a separate study.

3.2.1 Comparison between CHASER and OMI NO_2

581 Figure 7 compares the simulated and observed annual mean tropospheric NO_2 columns. The statistics for

582 the comparison are given in Table 5. The model captured the global spatial variation well with a spatial

583 correlation (*r*) of 0.70. The mean bias error (MBE) and the root mean square error (RMSE) are

584 respectively, 3×10^{14} and 5.4×10^{14} molecules cm^{-2}. On a global scale, CHASER estimations are

585 negatively biased by 38% compared to OMI. Actually, studies evaluating global NO_2 simulations with

586 satellite observations have reported similar negative biases (Miyazaki et al., 2012, Sekiya et al., 2018).

587 The differences in the spatial representativeness between the model and observations is one potential

588 reason for such negative biases. CHASER simulations at 1.1˚ improved the MBE and RMSE by 5 and

589 15%, respectively, compared to simulations at 2.8˚ (Sekiya et al. 2018). Moreover, Sekiya et al (2018)

590 used NO_2 simulations with an updated inventory and compared the results with OMI observations from

591 2014. Although they reported a better global spatial correlation (*r* > 0.90), the MBE (2.5×10^{14} molecules

592 cm^{-2}) and RMSE (4.4×10^{14} molecules cm^{-2}) values at 2.8˚ resolution are comparable to those obtained

593 from this study.

594   OMI retrievals show the highest NO_2 columns over eastern China (E-China) and Western Europe. Annual

595   mean NO_2 columns over the remainder of the land areas are between 7×10^{14} and 4×10^{15} molecules cm $^{-2}$.

596   Over the land areas the differences between the datasets are mostly between -2×10^{15} and 5×10^{14} molecules

597   cm^{-2}. Although CHASER also underestimates NO_2 columns over the ocean, the differences are lower than

598   that of over lands. CHASER estimates are higher by $\sim5\times10^{14}$ molecules cm^{-2} than OMI over Japan. Since

599   2012, the NO_2 columns have shown a declining trend over Japan, mainly because of emission controls in

600   China (Irie et al 2016). Probably because of simulations with an emission inventory earlier than 2012, the

601   simulated values tend to be higher than observations.

602   Figure 8 compares the seasonal variations in the monthly mean NO_2 columns in some selected region.

603   The error bars represent the 2-sigma standard deviation of the observed mean values. The numbers in

604   each subplot signify the regional spatial correlation between the datasets. Over eastern China (E-China),

605   CHASER values are negatively biased by 24%; the *r*-value is 0.68. The model captured the seasonality

606   well within variation range of the observations. Over E- and W-USA (eastern and western USA), the

607   respective *r*-values are 0.85 and 0.49 respectively. Simulated NO_2 columns are higher over E-USA than

608   over W-USA, consistent with the observations. Although, in both regions model estimates are biased by

609    $\sim23\%$ in the lower side compared to OMI observations, the RMSE in E-USA are $\sim40\%$ higher than in W-

610   USA.

611   Over Europe, CHASER estimates are negatively biased by 54%, with an *r*-value and RMSE of 0.80 and

612   1.28×10^{15} molecules cm^{-2}, respectively. The observed NO_2 levels over Europe are almost twice those of

613   the W-USA. The model was unable to capture the regional differences. Model underestimations in Europe

614   can be attributed to the older anthropogenic emission inventory used for the study. In fact, using the HTAP

615   2010 inventory the MBE (-0.53×1015 molecules cm^{-2}) between OMI and CHASER NO_2 column

616

617
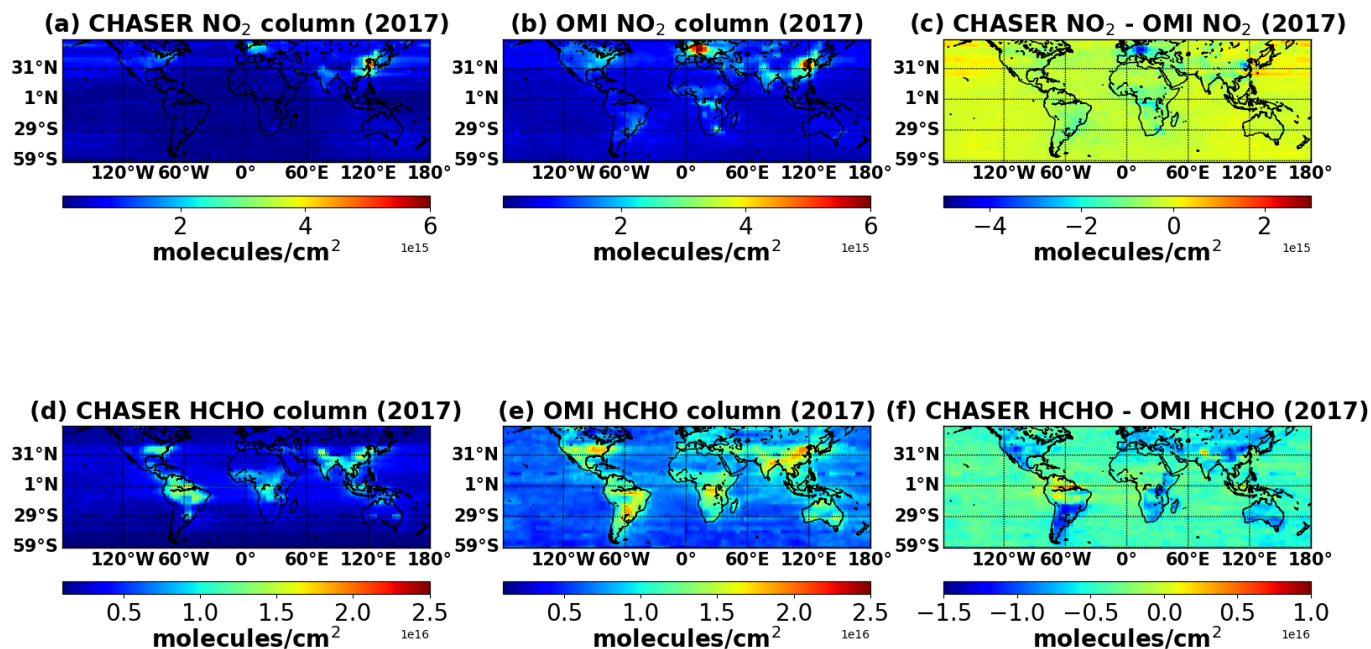
Figure 7: (top panel) Annual mean tropospheric NO_2 ($\times 10^{15}$ molecules cm^{-2}) columns (a) simulated by CHASER and (b) retrieved from OMI observations. Limited NO_2 data in July and December met the filtering criteria, thus discarded from the calculation. (c) The differences between the simulated and observed NO_2 columns. (bottom panel) Annual mean HCHO ($\times 10^{16}$ molecules cm^{-2}) columns (d) simulated by CHASER and (e) retrieved from OMI observations. (f) The differences between the simulated and observed HCHO columns. The data for 2017 are plotted only. All the datasets are mapped onto a 2.8˚ bin grid.

simulations at 2.8 over Europe (Sekiya et al. 2018) was ~ 50% lower than in the current study, although their RMSE value is similar.

627 Over India, MBE and RMSE for the annual mean NO_2 column are -4.3×10^{14} and 4.4×10^{14} molecules

628 cm^{-2}, respectively, and the *r*-value is moderate (0.65). Although CHASER estimates are negatively biased

629 by

630

631

632

633 **Table 5:** Statistics of comparison of annual mean NO2 and HCHO columns between CHASER and OMI.MBE1

634 and MBE2 are the respective mean bias error. RMSE1 and RMSE2 are the respective root mean square errors. r1

635 and r2 signifies the respective spatial correlation coefficient. The units of MBE1 and RMSE1 are $\times 10^{15}$ molecules

636 cm^{-2}. MBE2 and RMSE2 values are in the unit of $\times 10^{16}$ molecules cm^{-2}.

Region	r1 (CHASER vs OMI NO$_2$)	MBE1 (CHASER - OMI NO$_2$)	RMSE1 (CHASER – OMI NO$_2$)	r2 (CHASER vs OMI HCHO)	MBE2 (CHASER – OMI HCHO)	RMSE2 (CHASER – OMI HCHO)
Global	0.73	-0.30	0.54	0.74	- 0.45	0.49
E-China	0.68	-1.84	2.47	0.57	-0.63	0.64
E-USA	0.85	-0.62	0.63	0.91	-0.56	0.56
W-USA	0.49	-0.33	0.37	0.63	-0.71	0.71
Europe	0.80	-1.20	1.28	0.51	-0.67	0.68
India	0.65	-0.43	0.44	0.73	-0.56	0.57
N-Africa	0.58	-0.88	0.90	0.65	-0.29	0.32
S-Africa	0.80	-1.25	1.40	0.22	-0.66	0.70
S-America	0.87	-0.80	0.88	0.47	-0.31	0.40
SE Asia	0.57	-0.61	0.64	0.48	-0.41	0.44

637

638

639 32%, the values lie within the 2-sigma range of the observations. Sekiya et al. (2018) found no significant

640 effect of higher model resolution on the MBE and RMSE in the Indian region.

641 Over N- and S-Africa (North and South Africa), the model values are biased low by more than 75%

642 compared to the observations. Prominent biomass burning occurs in both regions, which explains the

643 enhanced NO_2 levels in the OMI retrievals. High negative biases in the model values indicates that

644 biomass burning NO_x emissions for the African regions are likely underestimated. Similarly, CHASER

645 underestimates NO_2 columns by 80% in South America, where pyrogenic emissions contributions are

646 significant. CHASER estimates are lower than OMI in these regions, but model captured the spatial

647 distribution well.

648 Over the SE-Asian (Southeast) region, OMI columns are enhanced during the dry season (i.e., January -

649 April. Burning agricultural wastes is a common practice in many countries in Southeast Asia during the

650 dry season, explaining the enhanced columns. The MBE (- 6×10^{14} molecules cm^{-2}) and RMSE (6.4 $\times$

651 10^{14} molecules cm^{-2}) in the SE-Asia region are lower than the African regions (i.e., N-Africa, S-Africa,

652 and S-America), where biomass burning is prominent.

653

654
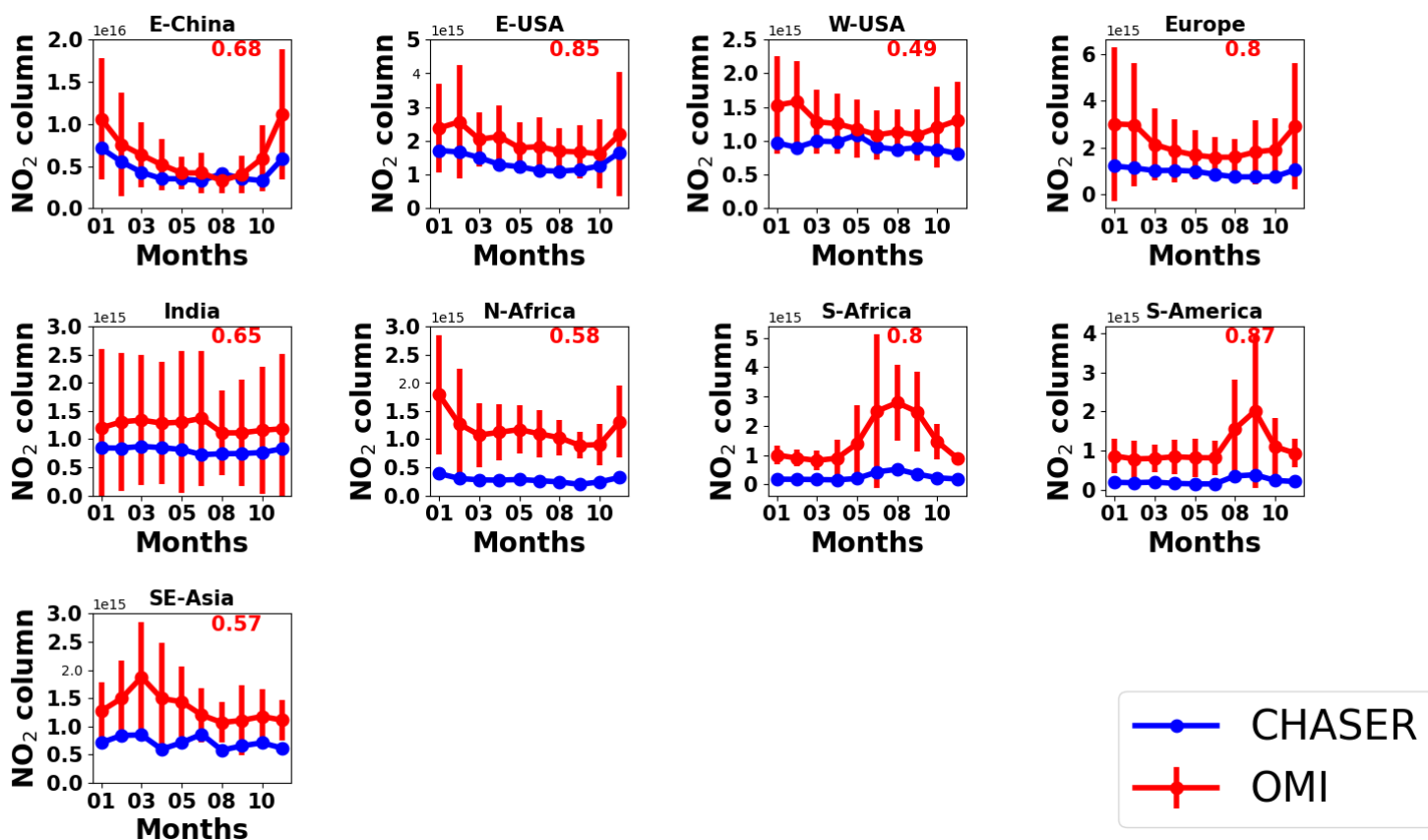
Figure 8: Seasonal variations in tropospheric NO_2 columns in E-China (110˚ -123˚ E, 30˚ – 40˚ N), E-USA (32˚ – 43˚ N, 71˚ – 95˚ W), W-USA(32˚ – 43˚ N, 100˚ – 125˚ W), Europe (35˚ – 60˚ N, 0˚ – 30˚ E), India (7.5˚ – 54˚ N, 68˚ – 97˚ E), N-Africa (5˚ – 15˚ N, 10˚ W – 30˚ E), S-Africa (5˚ -15˚ S, 10˚ -30˚ E), S-America (0˚ -20˚ S, 50˚ - 70˚ W), and SE-Asia (10˚ – 20˚ N, 9˚ – 145˚ E). CHASER simulations and OMI retrievals are plotted in blue and red colors respectively. The error bars indicate the 2-sigma variation of the observed mean values. The number in the insets signifies the regional spatial correlation between CHASER and OMI NO_2 columns.

3.2.2 Comparison between CHASER and OMI HCHO

Figure 9 presents a comparison between the simulated and observed global annual mean HCHO columns. The statistics of the comparison are given in Table 5. CHASER is able to reproduce the observed global spatial variation well with $r = 0.73$. The global MBE and the RMSE are respectively, -4.5×10^{15} and 4.9

666 $\times 10^{15}$ molecules cm^{-2}. MBE and RMSE for monthly mean fields show no distinctive seasonal variation

667 (Table S2). High HCHO columns are observed over China, Australia, Europe, India, Central Africa, South

668 America, and the United States. The model mostly underestimated the HCHO abundances in the higher

669 latitudes and Australia. Absolute differences between the model and observations in the higher latitudes

670 vary between 5×10^{15} and 1×10^{16} molecules cm^{-2}. Figure 9 compares the seasonal variations in the monthly

671 mean HCHO columns in some selected region. Therein error bars represent the 2-sigma standard

672 deviation of the observed mean values. The numbers in the respective subplots signify the regional spatial

673 correlation between the datasets.

674 Over E-China, CHASER HCHO estimates are negatively biased by 45% compared to OMI and the *r*-

675 value is greater than 0.50. The model reproduced the observed HCHO seasonality well including

676 enhanced peaks during the summer. The greatest differences between the datasets are observed during

677 the winter. Over E-USA, the spatial correlation between the datasets is greater than 0.90. Also, the

678 CHASER estimates are biased by 49% in the lower side. Simulations show that the peak in the HCHO

679 abundances occurs in July, which is consistent with the observations. The observed and simulated

680 magnitude of the seasonal modulation is 51 and 78%, respectively. The seasonality in the HCHO columns

681 in E-China and E-USA signifies a strong contribution from biogenic emissions. In both regions, the

682 observed peak HCHO column is ~ 1.75×10^{16} molecules cm^{-2}. The simulated peak HCHO values are also

683 similar in both regions, despite the underestimation. Over W-USA and Europe, the negative biases in the

684 simulation are greater than 60%. However, the simulated peaks during summer are consistent with the

685 observations. The OMI retrievals show that the HCHO abundances in both regions are almost similar,

686 which has been well captured by CHASER, although the magnitude is underestimated.
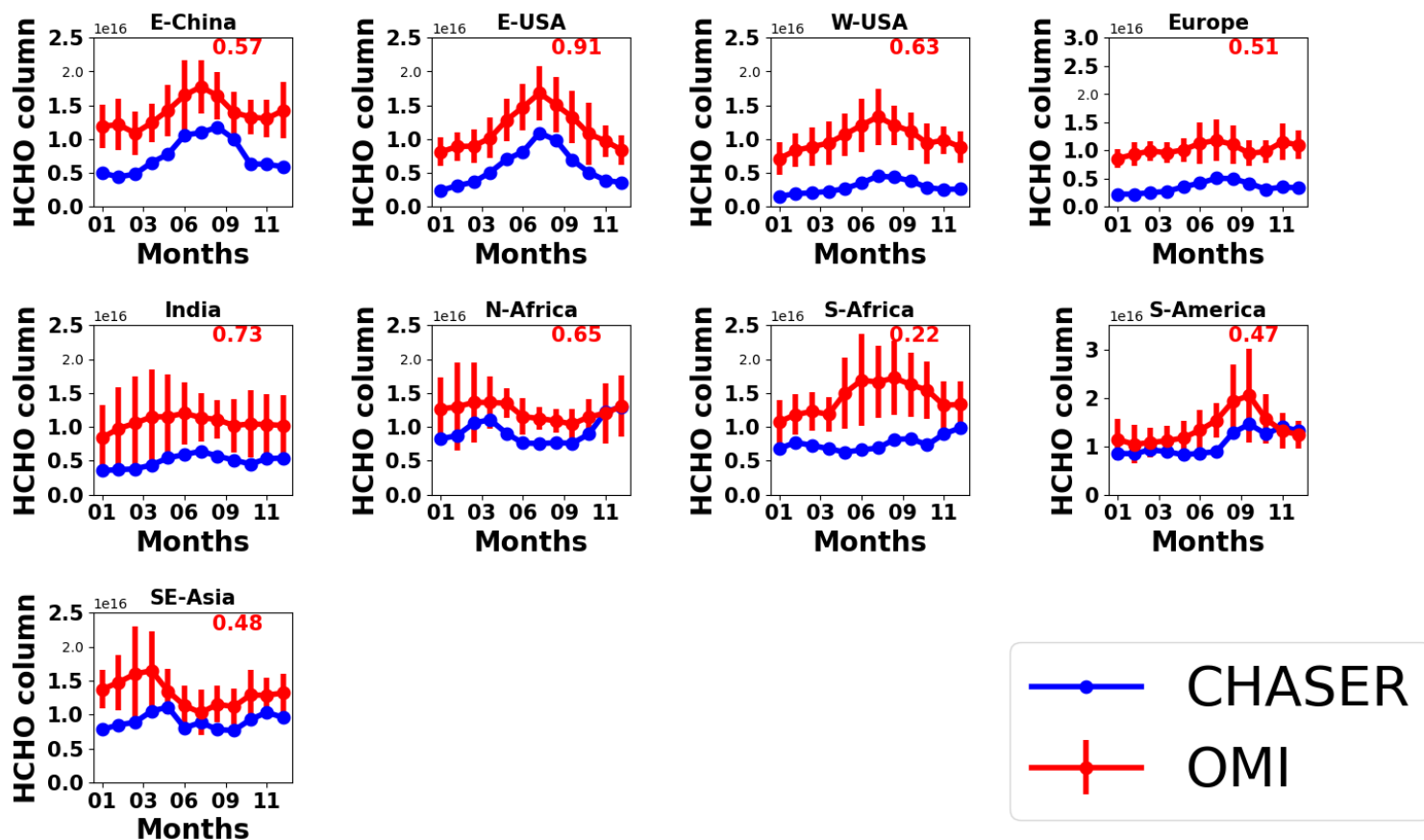
Figure 9: Seasonal variations in HCHO columns in E-China (110˚ -123˚ E, 30˚ – 40˚ N), E-USA (32˚ – 43˚ N, 71˚ – 95˚ W), W-USA(32˚ – 43˚ N, 100˚ – 125˚ W), Europe (35˚ – 60˚ N, 0˚ – 30˚ E), India (7.5˚ – 54˚ N, 68˚ – 97˚ E), N-Africa (5˚ – 15˚ N, 10˚ W – 30˚ E), S-Africa (5˚ -15˚ S, 10˚ -30˚ E), S-America (0˚ -20˚ S, 50˚ -70˚ W), and SE-Asia (10˚ – 20˚ N, 9˚ – 145˚ E). CHASER simulations and OMI retrievals are plotted in blue and red colors respectively. The error bars indicate the 2-sigma variation of the observed mean values. The number in the insets signifies the regional spatial correlation between CHASER and OMI HCHO columns.

Over India, the model estimates mostly lie outside of the observational variation ranges, although, CHASER captured the spatial distribution well ($r = 0.73$). Magnitudes of the seasonal variation in both OMI and CHASER are around 32%. Between the two African regions, CHASER demonstrated better capability for reproducing HCHO distribution in N-Africa ($r = 0.65$). Negative model bias in N-Africa is

almost half (22%) that of S-Africa (46%). Observed N-African HCHO columns are mostly higher than 1.2×10^{16} molecules cm^{-2} during the biomass burning period (November - April). Although the modeled values are lower than the observed values, the year-end columns (November - December) are similar. Both datasets show low HCHO variation during May - September. Over the S-African region, the model capabilities were limited.

Over S-America, the negative bias (~22%) in the model estimates compared to the observations is similar to that of N-Africa. In addition to consistency in the year-end (November to December) columns, CHASER well reproduced the biomass burning-led enhancements. The observed and simulated magnitudes of seasonal modulation are 49 and 43%, respectively.

Over SE-Asia, CHASER reproduced the observed biomass burning-led enhanced HCHO columns during the dry season (January - April), however, the occurrence of the peak is inconsistent. As discussed in section 3.1, observed HCHO peaks related to biomass burning can vary depending on the fire numbers. The r-value (0.48) is moderate and model is biased by 30% in the lower side. The model negative biases in the biomass prone regions are lowest (<30%) among the discussed regions.

De Smedt et al. (2021) reported that cloud corrections can positively bias OMI HCHO columns up to 30% compared to Tropospheric Ozone Monitoring Instrument (TROPOMI) columns. Consequently, uncertainties in the observations are also likely to contribute to the observed negative biases. Comparison among CHASER, TROPOMI, and OMI HCHO columns is beyond the scope of this study. However, the effects of uncertainties in the satellite retrievals on the negative biases is discussed qualitatively and briefly. To demonstrate such effects, CHASER and TROPOMI HCHO columns for 2019 are compared in Fig S3. The simulation settings and emission inventories are similar to those explained in section 3.2.3. The comparison results are presented in Table S2. TROPOMI data has been processed following De Smedt et al. (2021). The CHASER and TROPOMI HCHO spatial distribution correlates strongly with r-value of 0.78. The values for MBE and RMSE are respectively, -2.3×10^{15} and 2.8×10^{15} molecules cm^{-2}. Compared to OMI and TROPOMI, CHASER HCHO columns are negatively biased, respectively, by 61 and 38%. The model biases are lower when compared to TROPOMI observations. Because of temporal differences in the two comparisons, the biases cannot be compared quantitatively. However, the differences in the biases signify that the observational uncertainties can strongly affect discrepancies

728 between the simulated and observed HCHO abundances. Moreover, using different cloud products may

729 introduce inconsistencies in the OMI BIRA-IASB retrievals (De Smedt et al., 2021), affecting the

730 comparison results. De Smedt et al. (2021) proposed to recalculate the OMI HCHO VCDS based on the

731 AMF information to minimize cloud-induced uncertainties. Such a detailed method will be evaluated in

732 our future studies.

733

734

3.3 Evaluation of CHASER simulations at the three sites

3.3.1 Evaluation of CHASER HCHO at Phimai and Chiba

737 The seasonally averaged observed and modeled HCHO profiles and partial columns in the 0 - 4 km

738 altitude range at Phimai and Chiba are presented in Fig. 10. The CHASER outputs smoothed with MAX-

739 DOAS averaging kernels (AK) are also depicted. The AK is applied following Franco et al. (2015). First,

740 the CHASER HCHO profiles are interpolated to the MAX-DOAS vertical grids. Next, the MAX-DOAS

741 AK information from individual retrieved profiles is seasonally averaged according to the climate

742 classifications of each site. Finally, the CHASER outputs on the coincident days are selected, and the

743 seasonally averaged AK is applied to the daily mean interpolated profile. Applying individual AKs to the

744 model outputs yielded similar results. The seasonally averaged AKs for both sites are shown in Fig S4.

745 The coincident days at Phimai and Chiba were respectively,690 and 668.

746 At Phimai, CHASER predicted the increase in the HCHO partial columns during the dry season and

747 well-reproduced the HCHO seasonality. The simulated and observed seasonality correlates strongly with

748 R-value of 0.96. The modeled monthly mean values during the dry season are found to be within the 1σ

749 standard deviation of the observed values, indicating that the pyrogenic emissions estimates used for the

750 simulations are reasonable. CHASER predicted a 41% increase in the HCHO column during January -

751 March, consistent with the observations (41%). CHASER overestimates the HCHO columns in both

752 seasons, and the mean bias error (MBE) (CHASER – MAX-DOAS) is lower (3.7×10^{15} molecules cm^{-2})

753 (Table 6) during the wet season. Although underestimated, the dry season smoothed column values are

754 within the 1σ range.
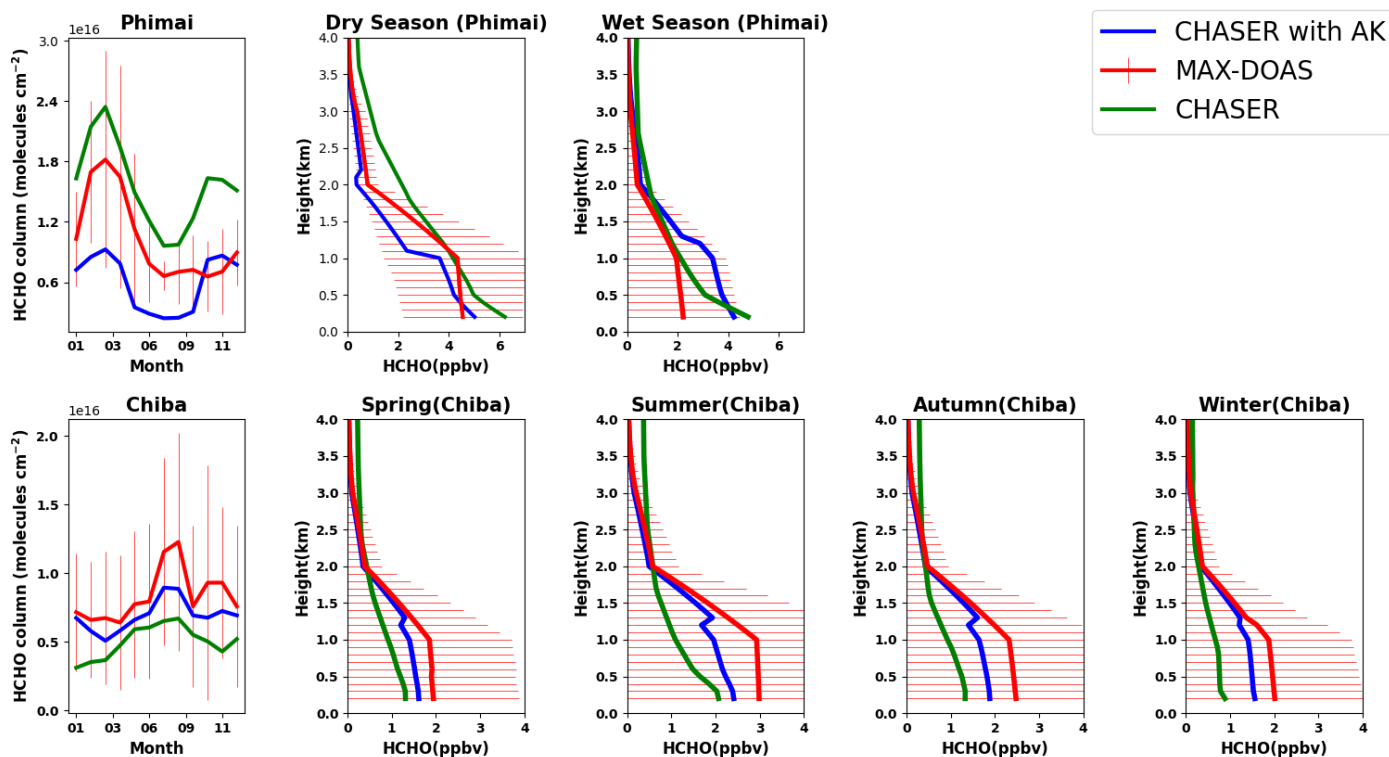
Figure 10. Seasonal variations in the HCHO partial columns at 0 - 4 km and vertical profiles during all seasons at Phimai and Chiba, as inferred from the MAX-DOAS observations (red) and CHASER simulation(green). The CHASER HCHO partial column and vertical profile smoothed with the MAX-DOAS AK are coloured blue. The AK information of all the screened (as explained in section 2.2) retrievals were averaged based on the seasonal classification of the respective sites. The coincident time and date between the model and observations are selected only. Error bars indicate the one sigma standard deviation of mean values of the MAX-DOAS observations.

The modeled and observed HCHO mixing ratios in the 1- 2km layers during the wet season are almost identical, whereas VMR near the surface (i.e., 0 - 1 km) differ by 30%. The absolute mean difference in the 0-4 km layer is ~0.45ppbv, with the maximum difference of 2.58 ppbv below 200 m. CHASER has demonstrated good capabilities for reproducing the HCHO profile in the 0.5 – 4 km layer during the wet season. The significance of AK information is low for the wet season. However, smoothing the model profiles reduces the overall MBE by 43%.

Table 6: Comparison of the seasonal mean HCHO partial columns and profiles (0-4 km) between MAX-DOAS and CHASER at Phimai and Chiba. MBE (CHASER – MAX-DOAS) is the mean bias error. The partial column and profile MBE units are respectively, $\times 10^{16}$ molecules cm^{-2} and ppbv, respectively.

Site	Season	Partial column MBE	Smoothed Partial column MBE	Profile MBE	Smoothed Profile MBE
Phimai	Overall	0.28	-0.07	0.35	0.01
Phimai	Dry	0.37	-0.28	0.58	-0.38
Phimai	Wet	0.21	0.07	0.45	0.33
Chiba	Overall	-0.12	-0.05	-0.37	-0.11
Chiba	Spring	-0.07	-0.04	-0.22	-0.12
Chiba	Summer	-0.16	-0.08	-0.45	-0.26
Chiba	Autumn	-0.10	-0.04	-0.40	-0.19
Chiba	Winter	-0.09	-0.01	-0.42	0.11

During the dry season, the respective absolute mean and maximum difference in the datasets in the 0-1 km layers is ~1 and ~2ppbv. The observed and simulated seasonal differences in the 0-1 km are 50 and 34%, respectively. Simulated dry season profile values at the heights greater than ~2 km is out of the 1σ variation range. The two-potential reasons for such differences are lower measurement sensitivity in the free troposphere and the overestimated Southeast Asian biogenic emissions in the model. Despite the measurement limitations, CHASER and MAX-DOAS wet season profiles up to 3 km are consistent. Consequently, it is likely that the biogenic emissions for this region in the model are overestimated. The Southeast Asian isoprene emissions in CHASER is 128 Tgyr^{-1}, higher than the CMAS-GLO-BIO (Sindelarova et al., 2022) inventory (78 Tgyr-1). However, the dry season HCHO profiles in 0 - 2 km are well simulated. Smoothing underestimates the dry season profile within the 1σ variation range but improved simulations below 200 m. At heights greater than 3 km, the smoothed values mostly reproduce the a priori because of reduced measurement sensitivity (i.e., low AK value, indicating limited information was retrievable).

Moderate correlation (R=0.58) can be observed between the modeled and observed HCHO partial columns at Chiba. CHASER was able to reproduce the peak in the partial columns in August. The model predicts a 41% increase in the HCHO columns during January - August, whereas the observed increase is 54%. Although Chiba is an urban site, the HCHO and temperature seasonal variations show a tight correlation (R~ 0.70) (Fig S5), suggesting that changes in biogenic emissions modulate HCHO seasonality. Similarly, the modeled seasonality is consistent with temperature variation (Fig. S4). Thus, the simulated HCHO seasonality in Chiba is reasonable, despite underestimation of absolute values. Smoothing the simulations improve the correlation, and the MBE is reduced by 54% (Table 6).

The CHASER HCHO profiles in the 0 - 4 km layers are lower than the observations, with an MBE of 0.39 ppbv. The absolute differences in the modeled and retrieved HCHO profiles in the 0-2 km layer during all seasons are higher than at Phimai. Absolute mean differences of ~ 1pbbv and higher are mainly observed for 0 to 2 km. In addition, the vertical gradients of the simulated profiles are low compared to those at Phimai. The modeled profiles at Chiba resemble the HCHO profiles measured over the ocean during the INTEX-B (Intercontinental Chemical Transport Experiment: Phase B) (Boeke et al., 2011). The Chiba site is near the sea, and coarse CHASER resolution includes the ocean pixels. Moreover, urban surfaces are not homogeneous. Thus, a significant part of the profile discrepancies is likely related to the systematic differences, in addition to emission estimates. However, the model estimates lie within the standard deviation range of the measurements. Because of the low gradients in the simulated profiles, the smoothed profiles mostly imitated the a priori values even below 2 km. Overall, given the large uncertainty on the MAX-DOAS profiles (Fig. 10), the differences between the observations and smoothed profile are statistically insignificant. Effects of the horizontal resolution on the simulated HCHO levels is discussed in section 3.3.4.

3.3.2 Evaluation of CHASER NO$_2$ in Phimai and Chiba

Figure 11 presents the seasonal averages of the MAX-DOAS and CHASER NO$_2$ profiles and partial columns (0 - 4 km) at Phimai and Chiba. The AK is applied to the modeled outputs for the Chiba site only.

816 Figure S5 of the supplementary information presents a comparison of the observations, model, and
817 smoothed model profiles averaged within the 0 - 2 km layer at Phimai. Smoothing with different a priori
818 values is depicted to demonstrate the effects of the a priori values. The smoothed NO_2 concentrations,
819 calculated using the original a priori values, show a seasonal variation shift. The mean smoothed profile
820 resembles the observations when a priori values are reduced by 50%; however, the dry season values are
821 similar in both cases. Two test cases of smoothing profiles using apriori values above 500 and 800 m
822 shows good agreement with the observations; however, the results are sensitive to the apriori values.
823 Because smoothed profiles are strongly biased to the apriori choice, the smoothing results obtained for
824 the Phimai site are discarded.

825 The modeled NO_2 partial column at Phimai shows good agreement with observations made during the
826 dry season. CHASER well reproduces the enhanced NO_2 columns attributable to biomass burning within
827 the standard deviation of the observations. The peak in the NO_2 levels during March is consistent in both
828 datasets. Although the seasonality does not agree in other months, the overall MBE is 8×10^{13} molecule
829 cm^{-2} (Table 7). Above 500 m, the datasets shows excellent agreement. The absolute mean differences in
830 the 0 - 1km layer are 0.22 ppbv, and the maximum difference of ~1.9 ppbv is observed near the surface.
831 Amidst the biomass burning influence, the NO_2 concentrations at Phimai are mostly < 1 ppbv. Thus, the
832 results of comparisons demonstrate CHASER's good capabilities in regions characterized by low NO_2
833 concentrations. Moreover, when NO_2 concentrations are less than < 1 ppbv, the AK information seems
834 less significant if the model can capture low-concentration scenarios.

835

837
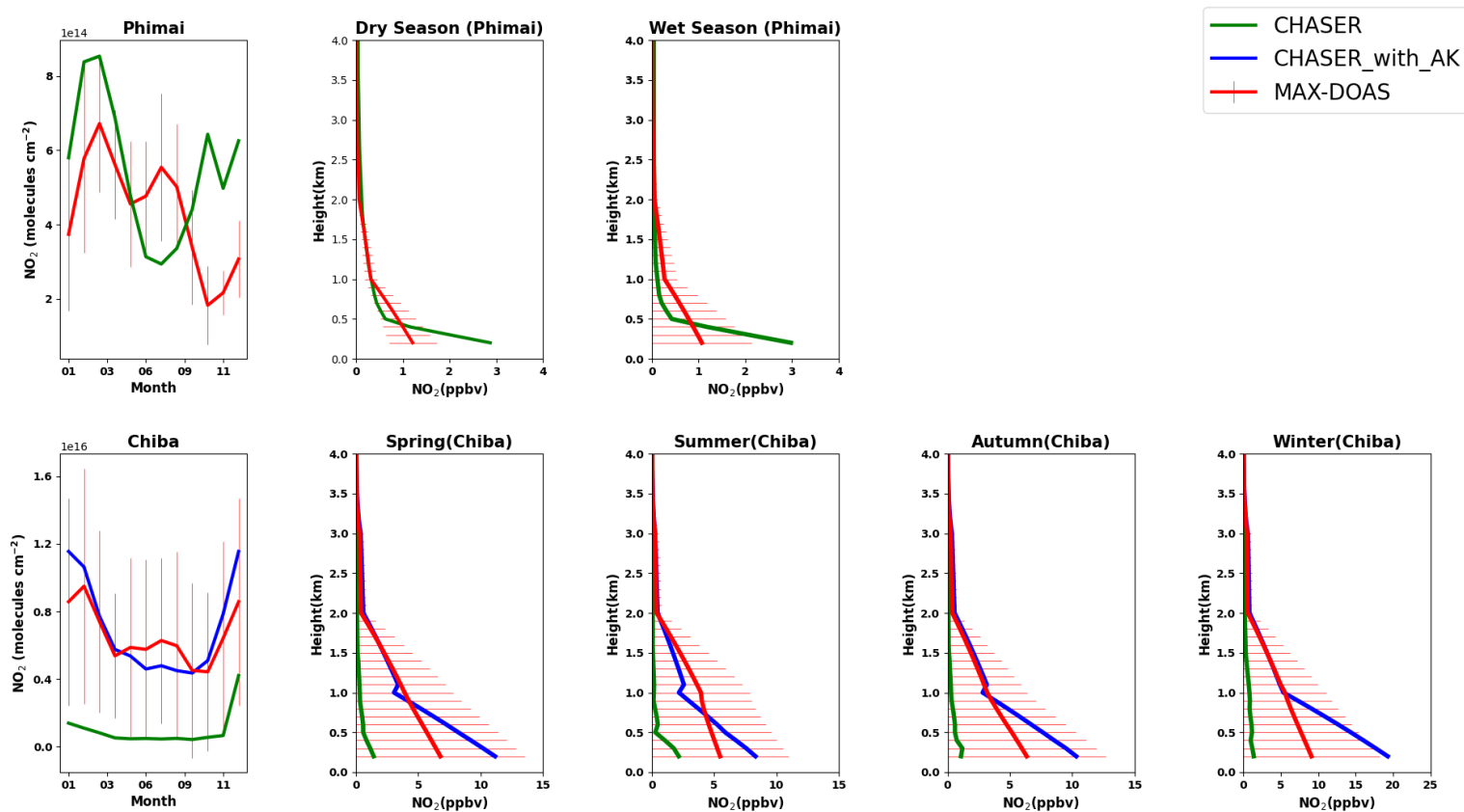
Figure 11. Seasonal variation in NO$_2$ partial columns from 0 - 4 km and vertical profiles during all seasons at Phimai and Chiba, as inferred from the MAX-DOAS observations (red) and CHASER simulation(green). The CHASER NO$_2$ partial column and vertical profile smoothed with the MAX-DOAS AK are coloured in blue. The coincident time and date between the model and observations are selected only. The error bars represent the one sigma standard deviation of mean values of the MAX-DOAS observations.

838
839
840
841
842
843
844
845
846
847

848 **Table 7:** Comparison of the seasonal mean NO_2 partial columns and profiles (0-4 km) between MAX-DOAS and
849 CHASER at Phimai and Chiba. MBE (CHASER – MAX-DOAS) is the mean bias error. The partial column and
850 profile MBE units are $\times 10^{15}$ molecules cm^{-2} and ppbv, respectively.

Site	Season	Partial column MBE	Smoothed Partial column MBE	Profile MBE	Smoothed Profile MBE
Phimai	Overall	0.08		0.11	
Phimai	Dry	0.18		0.09	
Phimai	Wet	-0.14		0.02	
Chiba	Overall	-5.58	-1.90	-3.27	-1.66
Chiba	Spring	-5.56	-2.00	-3.19	-1.74
Chiba	Summer	-5.52	-2.87	-2.85	-1.86
Chiba	Autumn	-4.57	-1.24	-2.74	-1.40
Chiba	Winter	-6.64	-1.50	-4.30	-1.63

851

852 Although the datasets are moderately correlated (R=0.59) at Chiba, the model largely underestimates the
853 NO_2 partial column with MBE of $\sim 5 \times 10^{15}$ molecules cm^{-2}. The model predicts almost constant NO_2
854 profiles and columns throughout the year. Therefore, the respective seasonal biases are almost similar.
855 The vertical gradient of the modeled NO_2 profiles is also low, too, similarly to the HCHO profiles. The
856 model resolution can be a potential cause for such significant underestimation. The AKs improved the
857 partial column and profiles significantly, reducing the MBE by more than 50%. However, the smoothed
858 profiles and partial columns between the 0 - 2 km layer, differ significantly from the simulations,
859 suggesting that the a priori values strongly affect the smoothed profiles. Consequently, the smoothed NO_2
860 profiles at Chiba (Fig.S7) are biased to the a priori values, similar to that of Phimai (Fig. S6). NO_2
861 smoothed profile sensitivity to a priori values might be attributable to our retrieval procedure. The a priori
862 data are taken from the measured SCD and retrieved VCD values. As a result, the values are sensitive in
863 the 0 - 2 km layer, similarly to the observations. Using a priori values other than those obtained from
864 observations can affect such sensitivity. The smoothing sensitivity to a priori values is stronger for NO_2
865 than HCHO. The NO_2 profile gradient is higher than that of HCHO (Figs. 10 and 11), which means that,

866   within 10 km (MAX-DOAS horizontal resolution), the NO_2 mixing ratio and a priori variability (sources

867   and sinks) is higher than those of HCHO, leading to a stronger a priori effect on the smoothed profiles.

868

869   The mean NO_2 mixing ratios in the 0 - 2 km layer in 2018, simulated at spatial resolutions of 2.8˚ × 2.8˚

870   (standard) and 1.4˚ × 1.4˚, are compared with observations at Chiba, as depicted in Fig.12. The error bars

871   are the 1σ standard deviation of the observations. Higher resolution simulations reduced the overall MBE

872   by 35% (Table 8). NO_2 concentrations at 1.4˚ are now within the variation range of the observations. The

873   1.4˚ simulation captured the NO_2 seasonal variability better than at 2.8˚. Despite improved resolution, the

874   model values are underestimated, with the highest MBE during the winter. According to Miyazaki et al.

875   (2020), the seasonality in the anthropogenic emissions, primarily wintertime heating, is not well

876   represented in the emission inventories, which could likely underestimate winter NO_2 levels. The best

877   agreement between the datasets is observed during summer and spring, with an MBE of ~1 ppbv on a

878   seasonal scale.

879
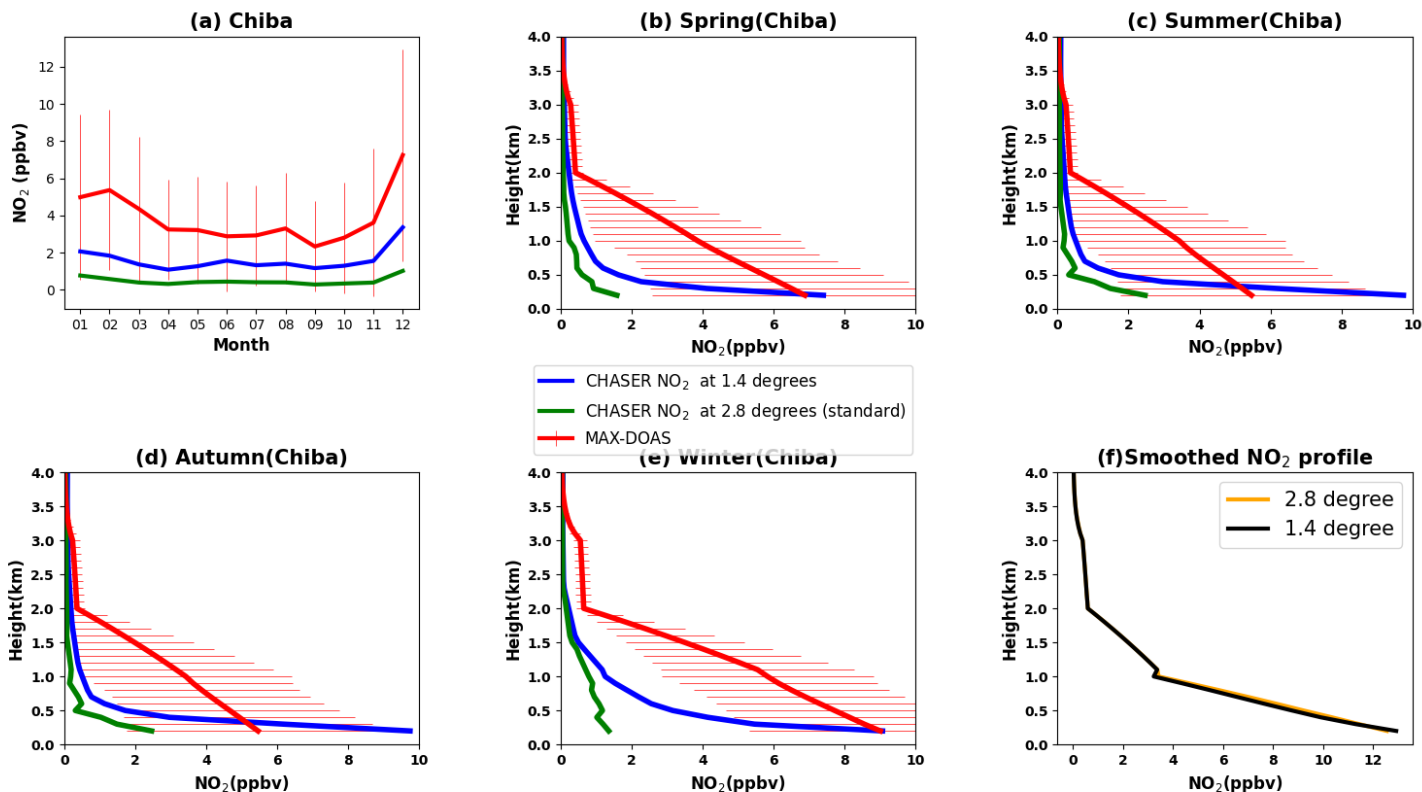
Figure 12: (a) Seasonal variations in the NO$_2$ mixing ratios in the 0 - 2 km layer at Chiba, as inferred from the MAX-DOAS observations (red) and two CHASER simulations at 2.8˚(green) and 1.4˚(blue) resolutions. The simulated NO$_2$ profiles at 2.8˚(green) and 1.4˚(blue) resolutions during (b) spring, (c) summer, (d) autumn, and (e) winter are shown with the observed seasonal profiles at Chiba. Only data (both observed and simulated) for 2018 are plotted. The coincident time and date between the model and observations are selected only. The error bars in (a), (b), (c), and (d) represent the one sigma standard deviation of mean values of the MAX-DOAS observations.

NO$_2$ profiles at 2.8˚ and 1.4˚ resolution are shown in Figs. 12(b - e). A strong effect of the increased resolution is observed below 500 m, reducing the negative bias by 70% near the surface. Above 500 m, the effects of higher resolution are limited, with an MBE reduction of 12% in the 0.6 – 2 km. Although the near-surface NO$_2$ concentrations at 1.4˚ resolution are overestimated, the values are within the standard deviation of the observations. At around 200m, winter mean NO$_2$ concentrations at 1.4˚

893 resolution are identical to the observations (~9 ppbv), and the summer mean is overestimated. Moreover,
894 the NO_2 levels above 2 km are similar at both resolutions. The resolution effects on NO_2 profiles vary
895 with the location and season (Williams et al., 2017). For example, CHASER NO_2 at 1.1˚ resolution
896 improved the agreement with aircraft observations below 650 hPa significantly over the Denver
897 metropolitan area (Sekiya et al. 2018), whereas, at Chiba, the 1.4˚ resolution improved the surface
898 estimates. Consequently, the horizontal resolution is not the only reason for the model underestimation.
899 Other factors such as the vertical resolution, uncertainties in emission inventories, and chemical kinetics,
900 can also affect the simulated NO_2 estimates. Effects of the emission inventory is discussed in section
901 3.3.4.

902 Figure 12(f) shows the smoothed NO_2 profiles at both resolutions. Although the profile shapes are
903 different, the smoothed profiles are almost identical, which demonstrates that, smoothed NO_2 profile
904 sensitivity to a priori choice is mostly independent of the model resolution.

905

906 **Table 8:** Comparison of the seasonal mean NO_2 profiles (0-2 km) among MAX-DOAS and CHASER simulations
907 at 2.8˚ and 1.4˚ resolutions at Chiba. MBE at (CHASER – MAX-DOAS) 1.4˚ and 2.8˚ are the mean bias error at
908 the respective resolutions. The MBE unit is ppbv.

Season	MBE at 1.4˚	MBE at 2.8˚
Overall	-2.24	-3.37
Spring	-2.26	-3.23
Summer	-1.50	-2.47
Autumn	-1.57	-2.57
Winter	-3.44	-5.07

909
910
911
912
913

3.3.3 Evaluation of CHASER HCHO in the IGP region

The IGP is the most fertile region in South Asia, which accounts for approximately 50% of the total agricultural production of India and is one of the significant contributing regions to the global greening based on leaf area index (Sarmah et al., 2021). Moreover, IGP is one of the regional HCHO hotspots in India (Chutia et al., 2019). The observed HCHO seasonality at Pantnagar is consistent with that reported by Mahajan et al. (2015) for the entire IGP region. Consequently, comparison with the HCHO retrievals in Pantnagar can assess the model capability in the IGP region. The spatial representativeness is a limitation for comparison between a point measurement and regional simulations. Thus, the results are interpreted qualitatively. Because of the availability of a dataset with continuous observations, only the comparison for 2017 is shown in Fig. 13.
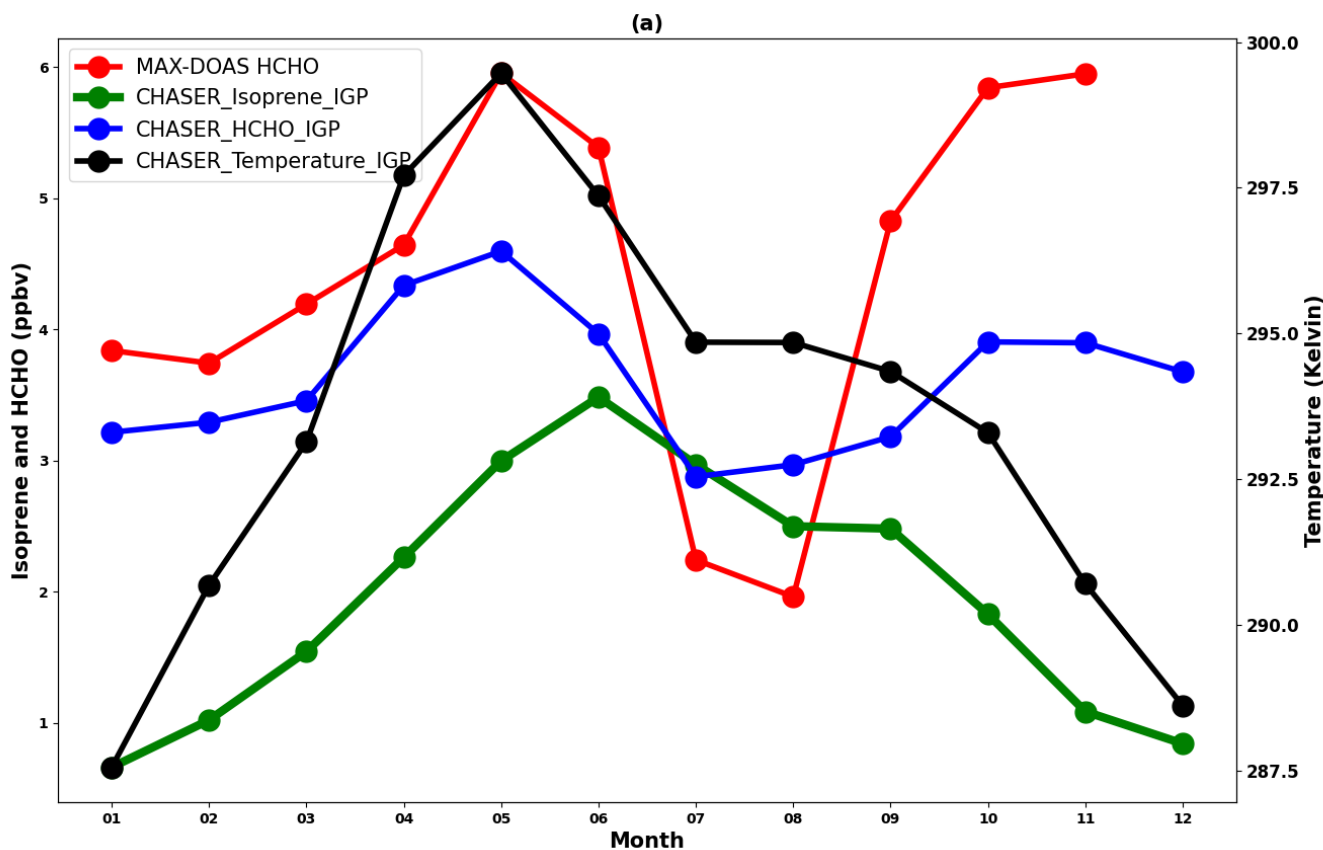
Figure 13. Seasonal variations in the MAX-DOAS (red) and CHASER (blue) HCHO concentrations at Pantnagar and the IGP region, respectively, in 2017. The coincident dates between the observations and model are plotted

only. The CHASER simulated isoprene and temperature seasonality are shown respectively, in green and black colours. Only the daytime simulated values were considered for the plot.

The modeled HCHO seasonal variations in the IGP region correlate well with the observations at Pantnagar ($R \sim 0.80$). The enhancement in the HCHO concentrations during the spring and post-monsoon season is well reproduced by CHASER, which indicates that CHASER can capture HCHO variation in complex terrain region such as IGP. Figure 13 also depicts the isoprene concentrations and temperature in the IGP region, in addition to the HCHO concentrations. Oxidization of precursor hydrocarbons and photochemical reactions are the most dominant sources of HCHO. Also, isoprene is the most abundant hydrocarbon in the atmosphere. The average ambient isoprene concentrations during July, August, and September in the IGP region are 1.4 ± 0.3 ppbv (Mishra et al., 2020). Therefore, the CHASER isoprene concentration range of $1.5 - 2$ ppbv during the monsoon season seems reasonable. The HCHO concentrations in the IGP region reach a peak during the spring and post-monsoon seasons. A strong correlation between HCHO, isoprene, and temperature variation ($R \sim 0.90$) during the first half of the year indicates that the change in biogenic emissions strongly drives the HCHO seasonal modulation. The observed enhancement in the HCHO levels during spring at Pantnagar is related to biomass burning. The biomass burning events are primarily concentrated in the northwest IGP region (Kumar and Sinha, 2021), where the site is located. On a regional scale, the biomass burning effects is expected to smear. Thus, the strong effect of the biogenic emission on the regional HCHO modulation is reasonable. HCHO modulation differs from isoprene and temperature during the post-monsoon period, suggesting a greater role of biomass burning and anthropogenic emissions. Consequently, the physical processes driving the HCHO seasonality in the IGP region are well reflected in the CHASER simulations.

3.3.4 Effects of the model resolution and emission inventories on results

Effects of the spatial resolution on the evaluation results is assessed by comparing the results of CHASER simulations at 2.8˚ and 1.4˚ resolutions with the surface observations, as shown in Fig. 14. Only, the simulated surface HCHO and NO_2 concentrations during 2017 are shown only. The statistics are provided in Table 9. For the Pantnagar site, only the simulations are presented. At Phimai, the HCHO simulations

differ by 3%. The standard simulation shows better agreement with the observations. The higher MBE at 1.4˚ occurred mostly because of the model overestimation during the wet season. The NO_2 mixing ratios at the two resolution differ by 9%. The MBEs for both trace gases at Phimai are less than 1 ppbv. Thus, the HCHO and NO_2 standard simulations at 2.8˚ can be regarded as reasonable for regions characterized by low NO_2 levels (<1 ppbv). At Chiba, surface NO_2 and HCHO mixing ratios at 1.4˚ resolution differ respectively, by 61 and 19%. The NO_2 MBE at 1.4˚ resolution improved significantly, indicating a strong effect of the model resolution. However, discussion in section 3.2.2 showed limited resolution-based improvement in the overall profile. Results for MBE in the HCHO mixing ratios at 1.4˚ mostly improved during summer. The wintertime HCHO estimates at both resolutions are similar. In contrast to Chiba and Phimai, differences in the HCHO simulations (30%) at Pantnagar are greater than those of NO_2 (3%). The effect of model resolution varying with location and season was also reported by Sekiya et al. (2018). Compared to the other two sites, differences in the NO_2 simulations at Chiba are larger. This finding is consistent with the results by William et al (2017), which found larger differences with changing model resolution over urban areas.

Although the NO_x estimates for the low NO_2 regions seem reasonable, global NO_x emissions have changed since 2008(i.e., EDGAR-HTAP (2008) emissions used for this study). A recent study by Miyazaki et al. (2020) reported changes in global NO_x emissions from 2005 to 2018. They found a continuous 30% increase in NO_x emissions in India since 2005. REAS v3 (Regional Emission inventory in Asia version 3) inventory estimated a 23% increase in NO_x emissions in India between 2010 - 2015, and power plants were the most significant contributor. Many power plants are clustered along the IGP region (Nair et al., 2007). Thus, the current simulation settings are likely to underestimate the NO_2 mixing ratios and columns in the IGP region. Figure S8 presents comparison of CHASER and OMI NO_2 columns for 2017 over the IGP region. Although the modeled columns are biased by 32% in the lower side, the spatial correlation between the datasets is high (r=0.78). CHASER values lie within the range of variation of the observations. Although underestimated, NO_2 estimates in the IGP based on the current inventory are yet reasonable. Sekiya et al., (2018) used higher model resolution and updated emission inventory (HTAP 2010 for simulations in 2014) and reported ~30% lower MBE over India. However, the RMSE values of both studies are comparable.

983   NO_x emissions in Japan have shown continuous decline since the execution of pollution control policies

984   in 1970 (Ohara et al., 2020). Irie et al. (2021) reported a declining trend in NO_2 levels in Chiba since

985   2012, echoing results obtained by Miyazaki et al. (2020) throughout Japan. The bias between CHASER

986   and OMI NO_2 column over Japan is non-significant (Fig. S8 and Table S3). Thus, an updated inventory

987   will not substantially affect the comparison results at the Chiba site. NO_x emissions increased

988   considerably in Southeast Asia. CHASER NO_2 estimates for Thailand based on HTAP 2008 inventory

989   are biased by 45% in the lower side compared to OMI (Fig. S8). However, Phimai being a rural site, the

990   NO_x levels are expected to be low. Changes in biomass burning NO_x estimates are likely to affect the

991   model estimates. Because, the NO_2 levels at Phimai are mostly less than 1 ppbv, the effect of updated

992   inventory on the comparison results is expected to be minimal.

993   CHASER HCHO columns over Japan, the IGP region, and Thailand are negatively biased respectively,

994   by 60, 36, and 32% compared to OMI observations, with r-values of 0.5 – 0.7 (Fig. S8). Surl et al. (2018)

995   reported spatial correlation of ~0.5 between GEOS-CHEM and OMI over the IGP region. Anthropogenic

996   VOC emissions in India and other Asian cities have increased since 2005, whereas a negative trend has

997   been observed over Japan (Bauwens et al., 2022). The REAS inventory estimated a 5% increase in

998   NMVOCS in India since 2005. Moreover, anthropogenic emission contributes strongly to the HCHO

999   abundances in the IGP region (Kumar and Sinha 2021). Thus, updated anthropogenic VOC emission

1000   inventory is likely to improve the model HCHO estimates in the study regions. However, the formation

1001   pathway of HCHO from isoprene emissions is a non-linear function of NO_x chemistry. Consequently, the

1002   effects of NO_x emissions changes on the overall HCHO simulations cannot be assessed based on current

1003   analyses explained herein.

1004
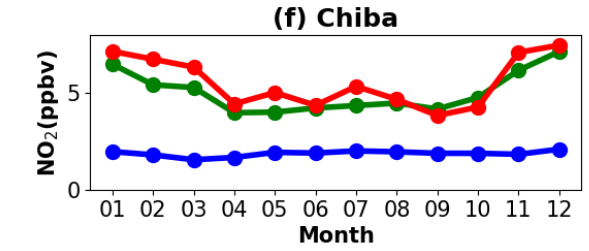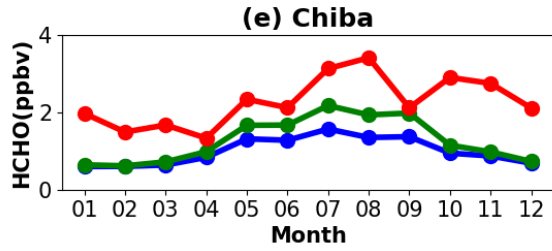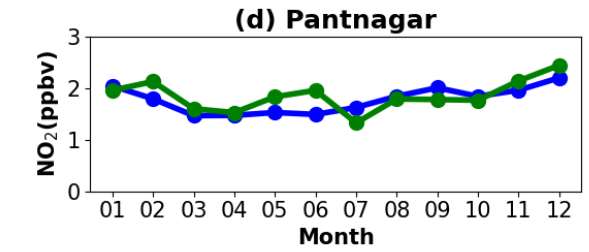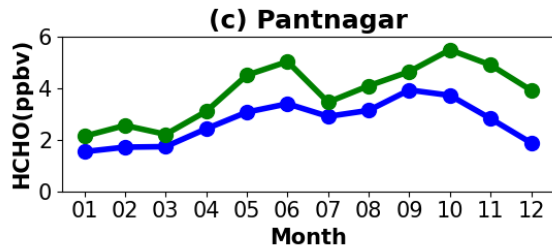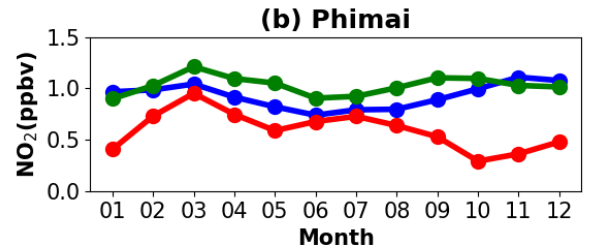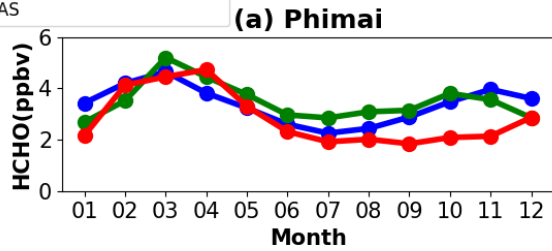
1005

1006

1007 **Figure 14.** Seasonal variation in the surface HCHO and NO₂ mixing ratios at (a & b) Phimai, (c & d) Pantnagar,

1008 and (e & f) Chiba simulated at spatial resolutions of 2.8° ×2.8° (blue) and 1.4° × 1.4°(green). Coincident MAX-

1009 DOAS NO₂ and HCHO VMRs in the 0-1 km layer at Phimai and Chiba are plotted in red. Observation at Pantnagar

1010 are discarded. Only the datasets for 2017 are plotted.

1011

1012

1013

1014

1015

1016

1017

1022 **Table 9:** The comparison between the observations and simulations at 2.8˚ and 1.4˚ spatial resolutions. The MBE
1023 is the mean bias error. The unit of MBE is ppbv.

Site	Trace gas	MBE at 2.8˚	MBE at 1.4˚	Differences between the simulations
Phimai	HCHO	0.54	0. 65	3%
Phimai	NO$_2$	0.33	0.43	9%
Chiba	HCHO	-1.27	-1.00	19%
Chiba	NO$_2$	-0.52	-3.69	61%
Pantnagar				30%
Pantnagar				3%

1024
1025
1026
1027

1028 **3.4 Contribution estimates**

1029 **3.4.1 Contribution from biomass burning to the HCHO and NO$_2$ abundances at Phimai**

1030 Good agreement between the datasets in the 0 - 1 km layer at Phimai can quantify biomass burning
1031 contributions to the HCHO and NO$_2$ concentrations. Figure 15 presents results of simulations L1_HCHO,
1032 L1_opt, and L1_NO$_2$. The simulation settings are presented in Table 3. For better readability, the
1033 switched-off emissions criterion is described in the legends of Fig.15. The plots present mean mixing
1034 ratios in the 0 – 1 km layer. Biomass burning contributes ~10% to the HCHO concentrations at Phimai
1035 during the dry season. However, based on the observations, a greater effect of biomass burning is
1036 expected. During the wet season, the MAX-DOAS and CHASER HCHO surface mixing ratios are,
1037 respectively, ~2 and ~4 ppbv (Fig. 10), indicating overestimation of the biogenic emissions in CHASER.
1038 Figure 15(b) shows the HCHO concentration obtained from simulation L1_opt and MAX-DOAS

observations in 2017. In the L1_opt simulation setting, the biomass burning emissions are switched off;
the biogenic emissions are optimized to reproduce results analogous to those obtained from observations
during the wet season. In the absence of biomass burning, the surface HCHO concentrations at Phimai
would be ~2 ppbv, indicating a biomass burning contribution of ~20–50% during the dry season. The
observed interseason difference in the HCHO concentration at Phimai is ~60%. Consequently, the revised
biomass burning contribution estimate is more reasonable. Pyrogenic emissions contributions to the NO_2
concentrations at Phimai are ~10% during the dry season (Fig. 15(c)). Because the NO_2 concentrations
are low at Phimai, the simulation results obtained for March, when the influence of biomass burning is
highest, are used to derive a better contribution estimate. In the absence of biomass burning, the NO_2
concentration during March would be about 0.84 ppbv (Fig.15(d)), indicating a contribution as high as
35% to the NO_2 concentrations at Phimai.
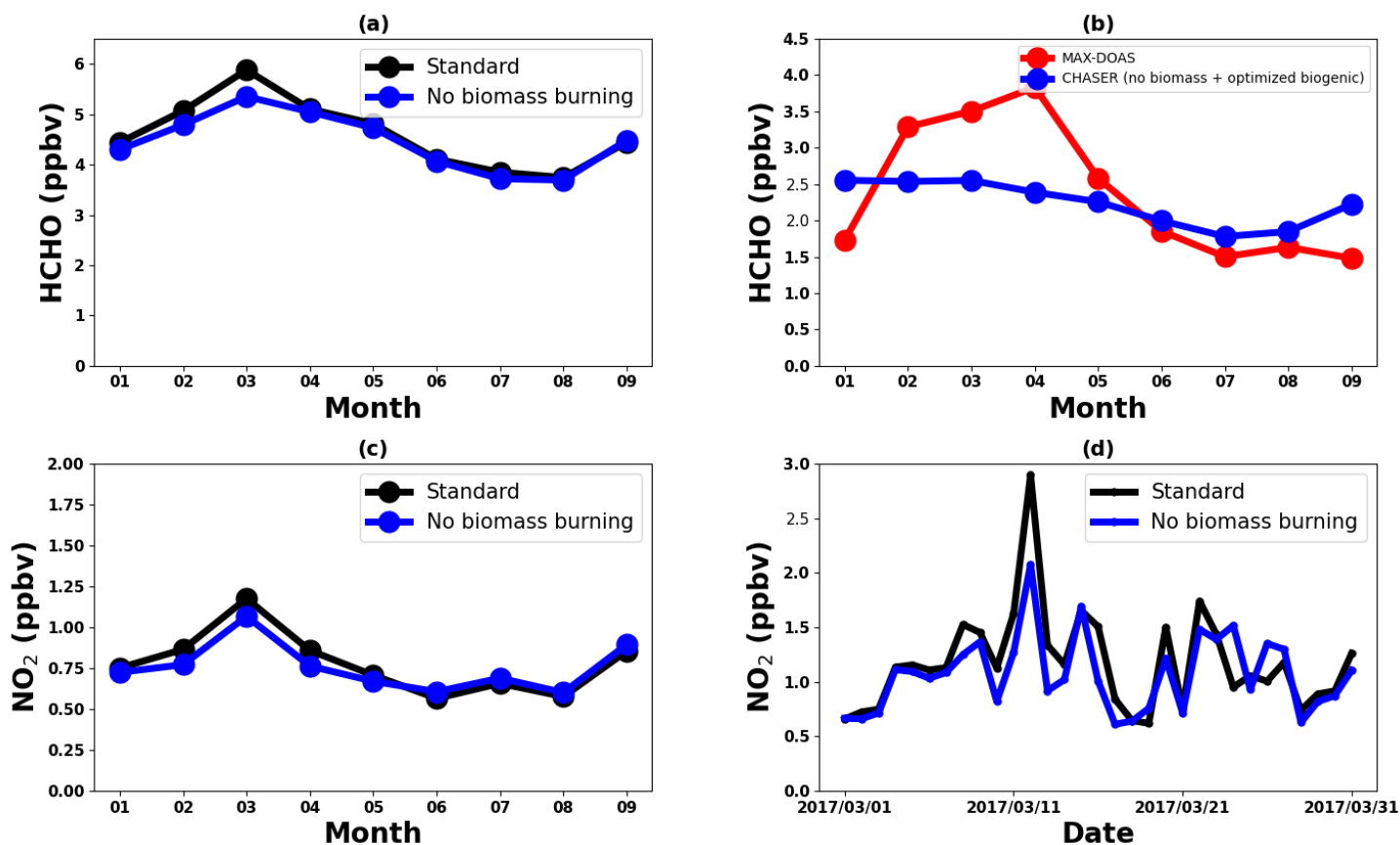
Figure 15. (top panel) (a) Seasonal variations in the HCHO concentrations in the 0 - 1 km layer at Phimai, as obtained from the standard and L1_HCHO simulations. Pyrogenic emissions of VOCs are switched off in L1_HCHO. (b) The HCHO seasonal variation in Phimai in 2017, as obtained from the MAX-DOAS observations (red) and L1_opt simulations. The pyrogenic VOC emissions were switched off, and the biogenic emissions were reduced by 50% in L1_opt. The coincident dates between the observation and the simulations are shown only. (bottom panel) (c) Seasonal variations in the NO_2 surface concentrations at Phimai in 2017, as obtained from the standard and L1_NO_2 simulations. (d) Standard and L1_NO_2 simulation outputs of the daily mean NO_2 surface concentrations during March 2017. The pyrogenic NO_2 emissions were switched off in the L1_NO_2 simulation. Only the daytime values from 09:00 – 15:00 LT are used to calculate the seasonal mean.

3.4.2 Contribution of soil NO_x emissions at Phimai

Because soil NO_x emissions are included in CHASER simulations, the NO_2 contributions from soil emissions are quantified. Figure 16 presents the monthly mean surface NO_2 concentrations at Phimai in 2017, simulated including (standard) and switching off (L1_NO_2) the soil NO_x emissions. The NO_2 concentrations between 09 and 12 hr. were used to calculate the monthly mean concentrations. Soil emissions contribute ~20% of the overall NO_2 concentrations at Phimai, with higher contributions during the wet season. The highest soil contribution of about 25% occurs in July.

3.4.3 Contribution from pyrogenic and anthropogenic emissions to the HCHO abundances in the IGP region

Figure 16(b) presents the standard, L1_HCHO (pyrogenic VOC emissions switched off), and L2 (anthropogenic VOC emissions switched off) HCHO simulations in the IGP region. According to L1_HCHO simulation results, effects of biomass burning emissions on the regional HCHO modulation are small (~12%). The HCHO concentrations in India have biogenic, anthropogenic, and pyrogenic VOC sources. However, biogenic VOCs are the primary driver of the over HCHO variation (Surl et al., 2018). Consequently, two reasons might be responsible for the small effects of pyrogenic emissions on HCHO concentrations: (1) Overestimation of the biogenic emission or underestimation of pyrogenic emissions

1080   in the model. (2) Stronger effects of anthropogenic VOC emissions than of pyrogenic VOCs. The L2

1081   simulations show that anthropogenic emissions contribute up to 30% of the HCHO concentration in the

1082   IGP region, with a maximum contributed during the post-monsoon season, which coincides with the

1083   lower isoprene concentration (i.e., biogenic emissions) and temperature (Fig. 14). Moreover, Kumar and

1084   Sinha (2021) reported high acetaldehyde concentrations from anthropogenic emissions in the IGP region

1085   throughout the year. Consequently, anthropogenic emissions are likely to be a significant driver of HCHO

1086   concentrations in the IGP region after biogenic emissions.

1087

1088
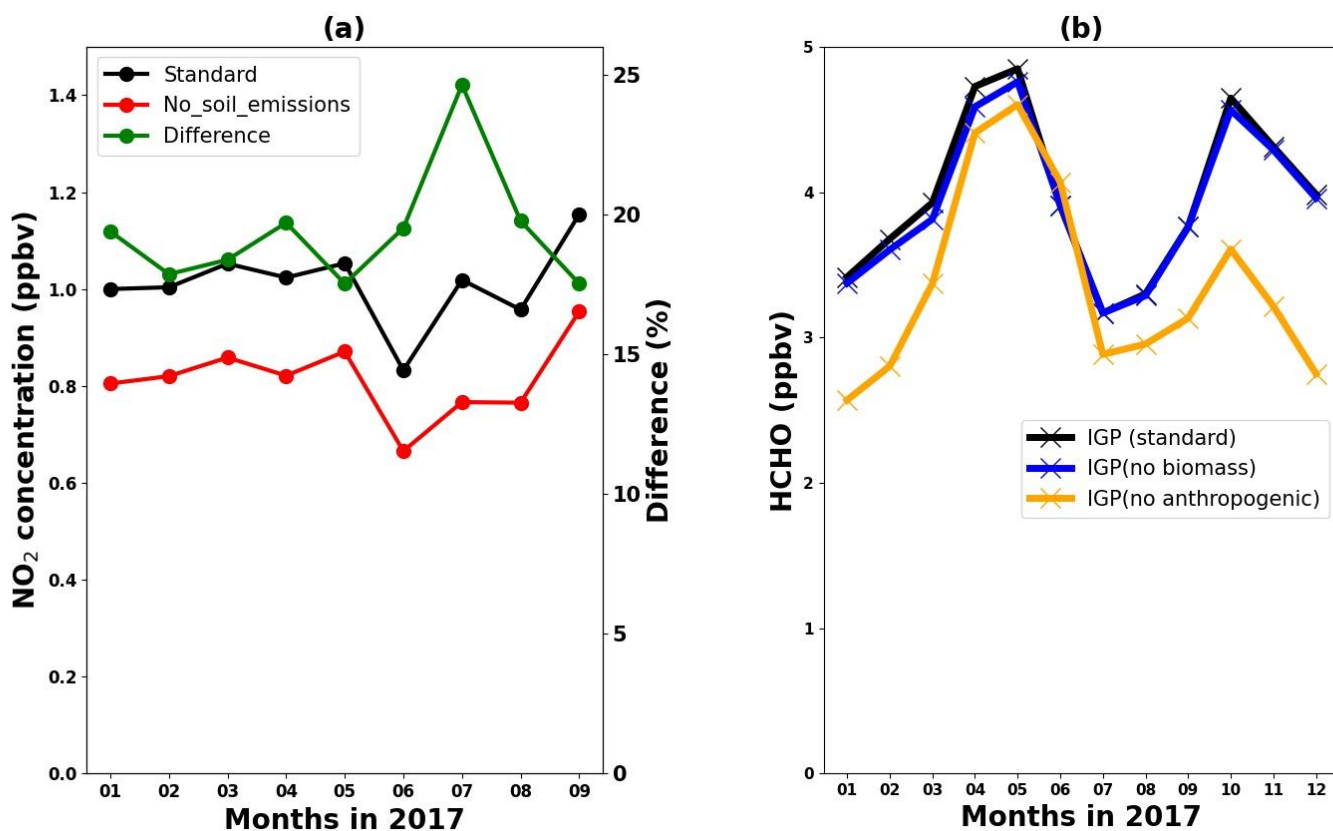
1089

1090 **Figure 16.** (a)Monthly mean NO_2 concentrations at Phimai were estimated from the standard (black) and L1_NO_2

1091 (red) simulations. The soil NO_x emissions are switched off in the LI_NO_2 simulation. The green line represents the

1092 percentage difference between the two simulations. (b) Seasonal variations in the HCHO concentrations in the IGP

region, obtained from the standard, L1_HCHO (pyrogenic VOC emission switched off), and L2 simulations (anthropogenic VOC emissions switched off). The simulations for 2017 are shown and analysed. Daytime values from 09:00-12:00 and 09:00 – 15:00 LT were selected respectively, for Phimai and IGP.

4 Conclusions

Using the JM2 algorithm, NO_2 and HCHO concentrations and profiles were retrieved from MAX-DOAS observations at three A-SKY sites during January 2017 - December 2018. The retrieved products were used to evaluate the global chemistry transport model CHASER simulations at the three sites. At all three locations, the seasonal variation of both trace gases was consistent throughout the investigated period. At Phimai and Pantnagar, biomass burning led to enhanced HCHO and NO_2 concentrations, respectively, during the dry season and spring and post-monsoon season. At Chiba, the HCHO variation was consistent with the temperature-led seasonal changes in biogenic emissions. The changes in the dry season HCHO and NO_2 levels at Phimai during 2015 - 2018 were consistent with the number of fire events.

The R_{FN} values were biased towards a particular regime when the standard transition range $1 < R_{FN} < 2$ (Duncan et al., 2010) was used. The parameterization of Souri et al. (2020) provides a better estimate of the transition region. The classification results of the revised transition region at Phimai and Pantnagar contradicted the results based on the standard transition range. However, they were more reasonable. Such a method based on observations, is therefore influenced by measurement constraints. More observational evidence must be accumulated to standardize this method. Overall, the results further indicated that that the standard transition region is not valid globally.

Despite the use of an old NO_x emission inventory the simulated NO_2 and HCHO spatial distributions agreed reasonably well with those observed from satellite- observations. The modeled regional NO_2 columns estimates were within the 2-sigma variability range of OMI NO_2 retrievals. Although the negative bias in HCHO comparison was higher than that of NO_2, the model demonstrated good capabilities for simulating the HCHO seasonal variation in different regions.

CHASER showed good capabilities at Phimai, characterized as a VOC-rich and low NO_2 (<1 ppbv) region. In both seasons, the observed and modeled profiles (HCHO and NO_2) agreed within the one sigma

standard deviation of the measurements, despite general overestimation of the model. Furthermore, both wet season HCHO profiles were almost identical in the 0.5 – 4 km layer in both datasets.

CHASER demonstrated limited performances at Chiba. NO_2 at higher resolution (i.e.,1.4˚) mainly improved the surface estimates, reducing the overall MBE in the 0 - 2 km layer by 35%. Finer resolution would improve the HCHO estimates in Chiba by 10%; however, it still is underestimated. Sensitivity studies for the Phimai site estimated biomass burning contributions to the respective HCHO and NO_2 concentrations of up to ~50 and ~ 35%, respectively. On average, 20% of the NO_2 level originates from soil NO_x emissions, increasing to 25% in July. Anthropogenic emissions (contribution of up to 30%) have a larger impact on VOC variation in the IGP region than biomass burning, which is consistent with earlier reports in the literature.

Code availability. The CHASER and JM2 source codes are not available publicly. Dr. Kengo Sudo (kengo@nagoya-u.jp) is the contact person for readers and researchers interested in the CHASER model. In addition, Dr. Hitoshi Irie (hitoshi.irie@chiba-u.jp) will answer queries related to the JM2 codes.

Data availability: The MAX-DOAS data used in the study are publicly accessible on the A-SKY network website (http://atmos3.cr.chiba-u.jp/a-sky/data.html). Upon request, the corresponding author can provide the CHASER simulations and MAX-DOAS averaging kernel data.

Author contributions: HMSH conceptualized the study, conducted the model simulations, analysed the observational and simulation data, and drafted the manuscript. AMF helped with the data processing. HI developed the JM2 code and maintained the A-SKY network. KS developed the CHASER model and supervised the study. MN is the PI of the Pantnagar site. AD and MN shared their experience to explain the results. HI, KS, AD, MN, and AMF commented and provided feedback on the final results and manuscript.

Conflict of Interest: The authors declare that they have no conflict of Interest

Acknowledgments: This research is supported by the Global Environmental Research fund (S-12 and S-20) of the Ministry of the Environment (MOE), Japan, and JSPS KAKENHI Grants: JP20H04320, JP19HO5669, and JP19H04235. The CHASER model simulations are partly performed with the supercomputer (NEC SX-Aurora TSUBASA) at the National Institute for environmental studies (NIES), Tsukuba, Japan. The authors are grateful to the OMI and TROPOMI data providers. Support from ISRO-ATCTM project for Pantnagar site is also acknowledged.

References

Amnuaylojaroen, T., Inkom, J., Janta, R., & Surapipith, V. : Long range transport of southeast asian pm2. 5 pollution to northern Thailand during high biomass burning episodes. Sustainability, 12(23), 10049. doi: https://doi.org/10.3390/su122310049, 2020

Arlander, D., Brüning, D., Schmidt, U., and Ehhalt, D. : The tropospheric distribution of formaldehyde during TROPOZ II, J. Atmos. Chem., 22(3), 251-269, https://doi.org/10.1007/BF00696637, 1995

Bauwens, M, Verreyken, B, Stavrakou, T, Müller, JF, & De Smedt, I. : Spaceborne evidence for significant anthropogenic VOC trends in Asian cities over 2005–2019. *Environ. Res. Lett., 17*(1), 015008. doi:https://iopscience.iop.org/article/10.1088/1748-9326/ac46eb/, 2022

Biswas, M. S., Ghude, S. D., Gurnale, D., Prabhakaran, T., and Mahajan, A. S. : Simultaneous Observations of Nitrogen Dioxide, Formaldehyde and Ozone in the Indo-Gangetic Plain. Aerosol Air Qual. Res., 19(8), 1749-1764, https://doi.org/10.4209/aaqr.2018.12.0484, 2019

Biswas, M. S., & Mahajan, A. S. : Year-long Concurrent MAX-DOAS Observations of Nitrogen Dioxide and Formaldehyde at Pune: Understanding Diurnal and Seasonal Variation Drivers. Aerosol Air Qual. Res., 21(6), 200524. doi:https://doi.org/10.4209/aaqr.200524 ,2021

1179

1180 Boeke, N. L., Marshall, J. D., Alvarez, S., Chance, K. V., Fried, A., Kurosu, T. P., Rappengluck, B., Richter,
1181   D.,Walega, J., & Weibring, P. : Formaldehyde columns from the Ozone Monitoring Instrument: Urban
1182   versus background levels and evaluation using aircraft data and a global model. J.Geophys.Res, 116(D5).
1183   2011

1184

1185

1186

1187 Bond, D. W., Zhang, R., Tie, X., Brasseur, G., Huffines, G., Orville, R. E., and Boccippio, D. J. : NO_x production
1188   by lightning over the continental United States, J. Geophys. Res., 106(D21), 27701-27710,
1189   https://doi.org/10.1029/2000JD000191, 2001

1190

1191 Bogumil, K., J. Orphal, T. Homann, S. Voigt, P. Spietz, O. Fleischmann, A. Vogel, M. Hartmann, H. Kromminga,
1192   and H. Bovensmann : Measurements of molecular absorption spectra with the SCIAMACHY pre-flight
1193   model: instrument characterization and reference data for atmospheric remote-sensing in the 230–2380 nm
1194   region, J. Photocho. Photobio. A, 157(2), 167-184, doi:10.1016/S1010-6030(03)00062-5, 2003

1195

1196

1197

1198

1199

1200 Burkert, J., Andrés-Hernández, M. D., Stöbener, D., Burrows, J. P., Weissenmayer, M., & Kraus, A. (2001) :
1201   Peroxy radical and related trace gas measurements in the boundary layer above the Atlantic Ocean, J.
1202   Geophys. Res., 106(D6), 5457-5477, https://doi.org/10.1029/2000JD900613, 2001

1203

1204

1205

1206 Cárdenas, L., Rondón, A., Johansson, C., & Sanhueza, E. : Effects of soil moisture, temperature, and inorganic
1207   nitrogen on nitric oxide emissions from acidic tropical savannah soils. J. Geophys. Res., 98(D8), 14783-
1208   14790, https://doi.org/10.1029/93JD01020, 1993

1209

1210 Chaliyakunnel, S., Millet, D. B., and Chen, X. : Constraining emissions of volatile organic compounds over the
1211   Indian subcontinent using space-based formaldehyde measurements. J. Geophys. Res., 124(19), 10525-
1212   10545, https://doi.org/10.1029/2019JD031262, 2019

1213

1214

1215 Chance, K. V., and R. J. D. Spurr. : Ring effect studies: Rayleigh scattering, including molecular
1216   parameters for rotational Raman scattering: and the Fraunhofer spectrum, *Appl. Opt.*, *36*(21),
1217   5224-5230 doi:10.1364/AO.36.005224,1997

1218

1219 Chutia, L., Ojha, N., Girach, I. A., Sahu, L. K., Alvarado, L. M. A., Burrows, J. P., Pathak., P., & Bhuyan, P. K. :
1220   Distribution of volatile organic compounds over Indian subcontinent during winter: WRF-chem simulation
1221   versus observations. Environ. Pollut., 252, 256-269. doi:https://doi.org/10.1016/j.envpol.2019.05.097,
1222   2019

1223

1224

1225

1226 Clémer, K., Van Roozendael, M., Fayt, C., Hendrick, F., Hermans, C., Pinardi, G., Spurr, R., Wang, P., and De
1227   Mazière, M. : Multiple wavelength retrieval of tropospheric aerosol optical properties from MAXDOAS
1228   measurements in Beijing, Atmos. Meas. Tech., 3(4), 863-878, https://doi.org/10.5194/amt-3-863-2010,
1229   2010

1230

1231

1232 Colella, P., & Woodward, P. R. : The piecewise parabolic method (PPM) for gas-dynamical simulations. J. Comput.
1233   Phys., 54(1), 174-201, https://doi.org/10.1016/0021-9991(84)90143-8, 1984

1234

1235

1236

1237

1238 Crutzen, P. J. : The influence of nitrogen oxides on the atmospheric ozone content. Q. J. Roy. Meteor. Soc., 96(408),
1239   320-325, https://doi.org/10.1002/qj.49709640815, 1970

1240

1241

1242 Davidson, E. A., Vitousek, P. M., Matson, P. A., Riley, R., García-Méndez, G., & Maass, J. M. : Soil emissions of
1243   nitric oxide in a seasonally dry tropical forest of Mexico. *J. Geophys. Res., 96*(D8), 15439-15445,
1244   https://doi.org/10.1029/91JD01476, 1991

1245

1246 De Smedt, I. , Pinardi, G., Vigouroux, C., Compernolle, S., Bais, A., Benavent, N., Eichmann, K-U., Hedelt, P.,
1247   Hendricks, F., Irie, H., Kumar, V., Lambert, J-C., Langerock, B., Lerot, C., Liu, C., Loyola, D., Piters, A.,
1248   Richter, A., Cardens, C.R., Romahn, F., Ryan, R.G., Sinha, V., Theys, N., Vlietinck, J., Wagger, T., Wang,
1249   T.,YU, H., and Van Roozendael, M.,: Comparative assessment of TROPOMI and OMI formaldehyde
1250   observations and validation against MAX-DOAS network column measurements. *Atmos. Chem. Phys.,*
1251   *21*(16), 12561-12593. doi:https://doi.org/10.5194/acp-21-12561-2021, 2021

1252

1253

1254

1255

1256

1257 Duncan, B. N., Yoshida, Y., Damon, M. R., Douglass, A. R., and Witte, J. C. : Temperature dependence of factors
1258   controlling isoprene emissions. Geophys. Res. Lett., 36(5), https://doi.org/10.1029/2008GL037090, 2009

1259

1260

1261 Emori, S., Nozawa, T., Numaguti, A., & Uno, I. : Importance of cumulus parameterization for precipitation
1262   simulation over East Asia in June. J. Meteorol. Soc. Jpn., 79(4), 939-947.
1263   https://doi.org/10.2151/jmsj.79.939, 2001

1264

1265

1266

1267

1268

1269 Fleischmann, O. C., M. Hartmann, J. P. Burrows, and J. Orphal : New ultraviolet absorption cross-sections of BrO
1270   at atmospheric temperatures measured by time-windowing Fourier transform spectroscopy, *J. Photocho.*
1271   *Photobio. A*, *168*(1), 117-132, doi:10.1016/j.jphotochem.2004.03.026, 2004

1272

1273

1274 Franco, B., Hendrick, F., Van Roozendael, M., Müller, J.-F., Stavrakou, T., Marais, E. A., Bovy, B., Bader, W.,
1275   Fayt, C., Hermans, C., Lejuene, B., Pinardi, G., Sevais, C., and Mahieu, E. : Retrievals of formaldehyde
1276   from ground-based FTIR and MAX-DOAS observations at the Jungfraujoch station and comparisons with
1277   GEOS-Chem and IMAGES model simulations. Atmos. Meas. Tech., 8(4), 1733-1756,
1278   https://doi.org/10.5194/amt-8-1733-2015, 2015

1279

1280 Fu, T. M., Jacob, D. J., Wittrock, F., Burrows, J. P., Vrekoussis, M., and Henze, D. K. : Global budgets of
1281   atmospheric glyoxal and methylglyoxal, and implications for formation of secondary organic aerosols, J.
1282   Geophys. Res., 113(D15), https://doi.org/10.1029/2007JD009505, 2008

1283

1284

1285 Frieß, U., Monks, P. S., Remedios, J. J., Rozanov, A., Sinreich, R., Wagner, T., & Platt, U. : MAX-DOAS O4
1286   measurements: A new technique to derive information on atmospheric aerosols: 2. Modeling studies. J.
1287   Geophys. Res., 111(D14), https://doi.org/10.1029/2005JD006618, 2006

1288

1289 Frieß, U., Klein Baltink, H., Beirle, S., Clémer, K., Hendrick, F., Henzing, B., Irie, H., de Leeuw, G., Li, A.,
1290   Moerman, M. M., van Roozendael, M., Shaiganfar, R., Wagner, T., Wang, Y., Xie, P., Yilmaz, S., and
1291   Zieger, P. : Intercomparison of aerosol extinction profiles retrieved from MAX-DOAS measurements.
1292   Atmos. Meas.Tech., 9(7), 3205-3222, https://doi.org/10.5194/amt-9-3205-2016, 2016

1293

1294 Fukushima, A., Kanamori, H., & Matsumoto, J. : Regionality of long-term trends and interannual variation of
1295   seasonal precipitation over India. Prog Earth Planet Sci, 6(1), 1-20. doi:https://doi.org/10.1186/s40645-
1296   019-0255-4, 2019
1297

1298

1299 Hak, C., Pundt, I., Trick, S., Kern, C., Platt, U., Dommen, J., Ordóñez, C., Prévôt, A. S. H., Junkermann, W.,
1300   Astorga-Lloréns, C., Larsen, B. R., Mellqvist, J., Strandberg, A., Yu, Y., Galle, B., Kleffmann, J., Lörzer,
1301   J. C., Braathen, G. O., and Volkamer, R. : Intercomparison of four different in-situ techniques for ambient
1302   formaldehyde measurements in urban air, *Atmos. Chem. Phys., 5*(11), 2881-2900.
1303   https://doi.org/10.5194/acp-5-2881-2005, 2005

1304

1305

1306

1307 Hall, S. J., Matson, P. A., and Roth, P. M. : NO_x emissions from soil: implications for air quality modeling in
1308   agricultural regions. Annu. Rev. Energy Environ., 21(1), 311-346.
1309   https://doi.org/10.1146/annurev.energy.21.1.311, 1996

1310

1311

1312 Halla, J. D., Wagner, T., Beirle, S., Brook, J. R., Hayden, K. L., O'Brien, J. M., Ng, A., Majonis, D., Wenig, M.
1313   O., and McLaren, R : Determination of tropospheric vertical columns of NO 2 and aerosol optical
1314   properties in a rural setting using MAX-DOAS. Atmos. Chem. Phys., 11(23), 12475-12498,
1315   https://doi.org/10.5194/acp-11-12475-2011, 2011

1316

1317

1318 Hendrick, F., Müller, J.-F., Clémer, K., Wang, P., De Mazière, M., Fayt, C., Gielen, C., Hermans, C., Ma, J. Z.,
1319   Pinardi, G., Stavrakou, T., Vlemmix, T., and Van Roozendael, M.: Four years of ground-based MAX-
1320   DOAS observations of HONO and NO_2 in the Beijing area, Atmos. Chem. Phys., 14(2), 765-781,
1321   https://doi.org/10.5194/acp-14-765-2014, 2014

1322

1323

1324 Hermans, C., A. Vandaele, S. Fally, M. Carleer, R. Colin, B. Coquart, A. Jenouvrier, and M.-F. Merienne.
1325 : Absorption cross-section of the collision-induced bands of oxygen from the UV to the NIR, in Weakly
1326 interacting molecular pairs: unconventional absorbers of radiation in the atmosphere, edited, pp. 193-
1327 202, Springer,2003.

1328

1329

1330

1331 Hönninger, G., Friedeburg, C. v., and Platt, U. : Multi axis differential optical absorption spectroscopy (MAX-
1332   DOAS), Atmos. Chem. Phys., 4(1), 231-254, https://doi.org/10.5194/acp-4-231-2004, 2004

1333

1334 Hoque, H.M. S., Irie, H., and Damiani, A. (2018). First MAX-DOAS Observations of Formaldehyde and Glyoxal
1335   in Phimai, Thailand. J. Geophys. Res., 123(17), 9957-9975, https://doi.org/10.1029/2018JD028480, 2018a

Hoque, H. M. S., Irie, H., Damiani, A., Rawat, P., and Naja, M. : First simultaneous observations of formaldehyde and glyoxal by MAX-DOAS in the Indo-Gangetic Plain region. *Sola*. , https://doi.org/10.2151/sola.2018-028, 2018b

Houweling, S., Dentener, F., and Lelieveld, J. : The impact of nonmethane hydrocarbon compounds on tropospheric photochemistry. J. Geophys. Res., 103(D9), 10673-10696, https://doi.org/10.1029/97JD03582, 1998

Huber, D. E., Steiner, A. L., & Kort, E. A. : Daily Cropland Soil NO_x Emissions Identified by TROPOMI and SMAP. Geophys. Res. Lett., 47(22), e2020GL089949, https://doi.org/10.1029/2020GL089949, 2020

Irie, H., Kanaya, Y., Akimoto, H., Iwabuchi, H., Shimizu, A., & Aoki, K. : First retrieval of tropospheric aerosol profiles using MAX-DOAS and comparison with lidar and sky radiometer measurements. Atmos. Chem. Phys., 8(2), 341-350, https://doi.org/10.5194/acp-8-341-2008, 2008a

Irie, H., Kanaya, Y., Akimoto, H., Tanimoto, H., Wang, Z., Gleason, J. F., & Bucsela, E. J. : Validation of OMI tropospheric NO_2 column data using MAX-DOAS measurements deep inside the North China Plain in June 2006: Mount Tai Experiment 2006. Atmos. Chem. Phys., 8(22), 6577-6586,https://doi.org/10.5194/acp-8-6577-2008, 2008b.

Irie, H., Kanaya, Y., Akimoto, H., Iwabuchi, H., Shimizu, A., & Aoki, K. : Dual-wavelength aerosol vertical profile measurements by MAX-DOAS at Tsukuba, Japan. *Atmos. Chem. Phys., 9*(8), 2741-2749, https://doi.org/10.5194/acp-9-2741-2009, 2009

Irie, H., Takashima, H., Kanaya, Y., Boersma, K., Gast, L., Wittrock, F., Brunner, D., Zhou, Y., Roozendael, M. V. : Eight-component retrievals from ground-based MAX-DOAS observations. Atmos. Meas. Tech., 4(6), 1027-1044, https://doi.org/10.5194/amt-4-1027-2011, 2011

Irie, H., Nakayama, T., Shimizu, A., Yamazaki, A., Nagai, T., Uchiyama, A., Zaizen, Y., Kagamitani, S., and Matsumi, Y. : Evaluation of MAX-DOAS aerosol retrievals by coincident observations using CRDS, lidar, and sky radiometer inTsukuba, Japan. Atmos. Meas.Tech., 8(7), 2775-2788, https://doi.org/10.5194/amt-8-2775-2015, 2015

Irie, H., Muto, T., Itahashi, S., Kurokawa, J., & Uno, I. : Turnaround of tropospheric nitrogen dioxide pollution trends in China, Japan, and South Korea. *Sola, 12*, 170-174. doi: https://doi.org/10.2151/sola.2016-035, 2016

Irie, H., Yonekawa, D., Damiani, A., Hoque, H.M.S, Sudo, K., & Itahashi, S.; Continuous multi-component MAX-DOAS observations for the planetary boundary layer ozone variation analysis at Chiba and Tsukuba, Japan, from 2013 to 2019. *Prog Earth Planet Sci, 8*(1), 1-11. doi:https://doi.org/10.1186/s40645-021-00424-9,2021

Ito, A., and Inatomi, M. : Use of a process-based model for assessing the methane budgets of global terrestrial ecosystems and evaluation of uncertainty. Biogeosciences, 9(2), 759-773. https://doi.org/10.5194/bg-9-759-2012, 2012

Iwabuchi, H. :Efficient Monte Carlo methods for radiative transfer modeling. J. Atmos. Sci., 63(9), 2324-2339, https://doi.org/10.1175/JAS3755.1, 2006

Jang, M., and Kamens, R. M. : Characterization of secondary aerosol from the photooxidation of toluene in the presence of NO_x and 1-propene, Environ. Sci. Technol., 35(18), 3626-3639. https://doi.org/10.1021/es010676+, 2001

Jin, X., Fiore, A. M., Murray, L. T., Valin, L. C., Lamsal, L. N., Duncan, B., Boersma, K.F., De Smedt, I., Abad, G.G., Chance, K., and Tonnesen, G. : Evaluating a space-based indicator of surface ozone-NOx-VOC

sensitivity over midlatitude source regions and application to decadal trends. J. Geophys. Res., 122(19), 10,439-410,461, https://doi.org/10.1002/2017JD026720, 2017

Jin, X., & Holloway, T. (2015). Spatial and temporal variability of ozone sensitivity over China observed from the Ozone Monitoring Instrument. J. Geophys.Res., 120(14), 7229-7246. doi: https://doi.org/10.1002/2015JD023250

Jenkin, M.E., Young, J.C., & Rickard, A.R. : The MCM v3. 3.1 degradation scheme for isoprene. Atmos. Chem. Phys., 15(20), 11433-11459. doi:https://doi.org/10.5194/acp-15-11433-2015, 2015

Joshi, H., Manish, N., Singh, K.P., Kumar,R., Bhardwaj, P., Babu, S.S., Satheesh, S.K., Moorthy, K.K., Chandola, H.C. : Investigations of aerosol black carbon from a semi-urban site in the Indo-Gangetic Plain region, Atmos. Environ., 125, 346-359, https://doi.org/10.1016/j.atmosenv.2015.04.007 ,2016.

K-1 model developers : K-1 Coupled GCM (MIROC) description, Tech .rep., Center for Climate System Research (University of Tokyo), National Institute for Environemntal Studies, and Frontier Research Center for Global Change, available at : http://ccsr.aori.u-tokyo.ac.jp/~hasumi/miroc_description.pdf, 2004

Kanakidou, M., Seinfeld, J. H., Pandis, S. N., Barnes, I., Dentener, F. J., Facchini, M. C., Van Dingenen, R., Ervens, B., Nenes, A., Nielsen, C. J., Swietlicki, E., Putaud, J. P., Balkanski, Y., Fuzzi, S., Horth, J., Moortgat, G. K., Winterhalter, R., Myhre, C. E. L., Tsigaridis, K., Vignati, E., Stephanou, E. G., and Wilson, J. : Organic aerosol and global climate modelling: a review. Atmos. Chem. Phys., 5(4), 1053-1123, https://doi.org/10.5194/acp-5-1053-2005

Kanaya, Y., Irie, H., Takashima, H., Iwabuchi, H., Akimoto, H., Sudo, K., Gu, M., Chong, J., Kim, Y. J., Lee, H., Li, A., Si, F., Xu, J., Xie, P.-H., Liu, W.-Q., Dzhola, A., Postylyakov, O., Ivanov, V., Grechko, E., Terpugova, S., and Panchenko, M.: Long-term MAX-DOAS network observations of NO_2 in Russia and Asia (MADRAS) during the period 2007–2012: instrumentation, elucidation of

climatology, and comparisons with OMI satellite observations and global model simulations. Atmos. Chem. Phys., 14(15), 7909-7927, https://doi.org/10.5194/acp-14-7909-2014, 2014

Kannari, A., Tonooka, Y., Baba, T., & Murano, K. : Development of multiple-species 1km× 1km resolution hourly basis emissions inventory for Japan. Atmos. Environ., 41(16), 3428-3439. doi:https://doi.org/10.1016/j.atmosenv.2006.12.015, 2007

Khodmanee, S., & Amnuaylojaroen, T., Impact of Biomass Burning on Ozone, Carbon Monoxide, and Nitrogen Dioxide in Northern Thailand. *Front. Enviorn. Sci., 9*, 27. doi:https://doi.org/10.3389/fenvs.2021.641877, 2021

Kreher, K., Van Roozendael, M., Hendrick, F., Apituley, A., Dimitropoulou, E., Frieß, U., Richter, A., Wagner, T., Lampel, J., Abuhassan, N., Ang, L., Anguas, M., Bais, A., Benavent, N., Bösch, T., Bognar, K., Borovski, A., Bruchkouski, I., Cede, A., Chan, K. L., Donner, S., Drosoglou, T., Fayt, C., Finkenzeller, H., Garcia-Nieto, D., Gielen, C., Gómez-Martín, L., Hao, N., Henzing, B., Herman, J. R., Hermans, C., Hoque, S., Irie, H., Jin, J., Johnston, P., Khayyam Butt, J., Khokhar, F., Koenig, T. K., Kuhn, J., Kumar, V., Liu, C., Ma, J., Merlaud, A., Mishra, A. K., Müller, M., Navarro-Comas, M., Ostendorf, M., Pazmino, A., Peters, E., Pinardi, G., Pinharanda, M., Piters, A., Platt, U., Postylyakov, O., Prados-Roman, C., Puentedura, O., Querel, R., Saiz-Lopez, A., Schönhardt, A., Schreier, S. F., Seyler, A., Sinha, V., Spinei, E., Strong, K., Tack, F., Tian, X., Tiefengraber, M., Tirpitz, J.-L., van Gent, J., Volkamer, R., Vrekoussis, M., Wang, S., Wang, Z., Wenig, M., Wittrock, F., Xie, P. H., Xu, J., Yela, M., Zhang, C., and Zhao, X.: Intercomparison of NO_2, O_4, O_3 and HCHO slant column measurements by MAX-DOAS and zenith-sky UV–visible spectrometers during CINDI-2. Atmos. Meas. Tech., 13(5), 2169-2208, https://doi.org/10.5194/amt-13-2169-2020, 2020

Kumar, V., Beirle, S., Dörner, S., Mishra, A. K., Donner, S., Wang, Y., Sinha,V., and Wagner, T. (2020). Long-term MAX-DOAS measurements of NO2, HCHO, and aerosols and evaluation of corresponding satellite data products over Mohali in the Indo-Gangetic Plain. Atmos. Chem. Phys., *20*(22), 14183-14235. doi:10.5194/acp-20-14183-2020

1467 Kumar, V., & Sinha, V. (2021), Season-wise analyses of VOCs, hydroxyl radicals and ozone formation chemistry
1468   over north-west India reveal isoprene and acetaldehyde as the most potent ozone precursors throughout the
1469   year. Chemosphere, *283*, 131184. doi:https://doi.org/10.1016/j.chemosphere.2021.131184
1470

1471

1472 Kurucz, R. L., Furenlid, I., Brault, J., and Testerman, L. : Solar Flux Atlas from 296 to 1300 nm.
1473   Natl. Sol. Obs., Sunspot, New Mexico, 240, 1984

1474

1475 Lee, M., Heikes, B. G., Jacob, D. J., Sachse, G., and Anderson, B. : Hydrogen peroxide, organic hydroperoxide,
1476   and formaldehyde as primary pollutants from biomass burning, J. Geophys. Res., 102(D1), 1301-1309,
1477   https://doi.org/10.1029/96JD01709, 1997

1478

1479

1480

1481

1482

1483

1484

1485

1486

1487 Lin, S.-J., & Rood, R. B. : Multidimensional flux-form semi-Lagrangian transport schemes. Mon. Weather Rev.,
1488   124(9), 2046-2070, https://doi.org/10.1175/1520-0493(1996)124<2046:MFFSLT>2.0.CO;2, 1996

1489

1490 Ma, J., Beirle, S., Jin, J., Shaiganfar, R., Yan, P., and Wagner, T. : Tropospheric NO_2 vertical column densities
1491   over Beijing: results of the first three years of ground-based MAX-DOAS measurements (2008–2011) and
1492   satellite validation,Atmos. Chem. Phys., 13(3), 1547-1567, https://doi.org/10.5194/acp-13-1547-2013,
1493   2013

1494

1495

1496 Mallik, C., & Lal, S. : Seasonal characteristics of SO_2, NO_2, and CO emissions in and around the Indo-Gangetic
1497   Plain, Environ Monit Assess, *186*(2), 1295-1310, https://doi.org/10.1007/s10661-013-3458-y,2015

1498

1499 Martin, R. V., Fiore, A. M., and Van Donkelaar, A. : Space-based diagnosis of surface ozone sensitivity to
1500   anthropogenic emissions, Geophys. Res. Lett., 31(6), https://doi.org/10.1029/2004GL019416, 2004

1501

1502

1503 Mahajan, A. S., De Smedt, I., Biswas, M. S., Ghude, S., Fadnavis, S., Roy, C., and van Roozendael, M. : Inter-
1504   annual variations in satellite observations of nitrogen dioxide and formaldehyde over India. Atmos.
1505   Environ., 116, 194-201, https://doi.org/10.1016/j.atmosenv.2015.06.004, 2015

1506

1507

1508

1509

1510

1511

1512

1513 Meller, R., and G. K. Moortgat. : Temperature dependence of the absorption cross sections of formaldehyde
1514   between 223 and 323 K in the wavelength range 225–375 nm, *J. Geophys. Res.*, *105*(D6), 7089-7101,
1515   doi:10.1029/1999JD901074, 2000

1516

1517

1518

1519 Mellor, G. L., & Yamada, T. : A hierarchy of turbulence closure models for planetary boundary layers. J. Atmos.
1520   Sci., 31(7), 1791-1806, https://doi.org/10.1175/1520-0469(1974)031<1791:AHOTCM>2.0.CO;2, 1974

1521

1522

1523 Mishra, A. K., and Sinha, V. : Emission drivers and variability of ambient isoprene, formaldehyde and
1524   acetaldehyde in north-west India during monsoon season, Environ. Pollut., 267, 115538,
1525   https://doi.org/10.1016/j.envpol.2020.115538, 2020

1526

1527 Miyazaki, K., Bowman, K., Sekiya, T., Eskes, H., Boersma, F., Worden, H., Livesey, N., Payne, V.H., Sudo, K.,
1528   Kanaya, Y., Takigawa, M., and Ogochi, K. (2020). Updated tropospheric chemistry reanalysis and

emission estimates, TCR-2, for 2005–2018. Earth Syst. Sci. Data, 12(3), 2223-2259. doi:10.5194/essd-12-2223-2020

Miyazaki, K., Eskes, H., Sudo, K., Boersma, K. F., Bowman, K., and Kanaya, Y. : Decadal changes in global surface NOx emissions from multi-constituent satellite data assimilation. Atmos. Chem. Phys., 17(2), 807-837, https://doi.org/10.5194/acp-17-807-2017, 2017

Morino, Y, Ohara, T, Yokouchi, Y, & Ooki, A. : Comprehensive source apportionment of volatile organic compounds using observational data, two receptor models, and an emission inventory in Tokyo metropolitan area. J. Geophys. Res., 116(D2),doi:https://doi.org/10.1029/2010JD014762, 2011

Nair, V. S., Moorthy, K. K., Alappattu, D. P., Kunhikrishnan, P.K., George, S., Nair, P. R., Babu, S.S., Abish, A., Satheesh, S.K., Tripathi, S. N., Niranjan, K., Madhavan, B.L., Srikant, V., Dutt, C.B.S., Badarinath, K>V>S., & Reddy, R.R.: Wintertime aerosol characteristics over the Indo-Gangetic Plain (IGP): Impacts of local boundary layer processes and long-range transport. J. Geophys. Res., 112(D13). doi:https://doi.org/10.1029/2006JD008099, 2007

Ohara, T., Akimoto, H., Kurokawa, J., Horii, N., Yamaji, K., Yan, X., & Hayasaka, T. : An Asian emission inventory of anthropogenic emission sources for the period 1980–2020. Atmos. Chem. Phys., 7(16), 4419-4444. doi:https://doi.org/10.5194/acp-7-4419-2007, 2007

Platt, U. : Differential optical absorption spectroscopy (DOAS), in Chemical Analysis Series, edited, pp. 27-84, Wiley & Sons. Inc., 1994

Platt, U., and Stutz, J. : Differential Optical Absorption Spectroscopy, Springer, 2008

Price, C., & Rind, D. : A simple lightning parameterization for calculating global lightning distributions. *J. Geophys. Res., 97*(D9), 9919-9933, https://doi.org/10.1029/92JD00719, 1992

Rodgers, C. D. : Inverse methods for atmospheric sounding: theory and practice, World scientific Singapore, 2008

1565 Roscoe, H. K., Van Roozendael, M., Fayt, C., du Piesanie, A., Abuhassan, N., Adams, C., Akrami, M., Cede, A.,
1566   Chong, J., Clémer, K., Friess, U., Gil Ojeda, M., Goutail, F., Graves, R., Griesfeller, A., Grossmann, K.,
1567   Hemerijckx, G., Hendrick, F., Herman, J., Hermans, C., Irie, H., Johnston, P. V., Kanaya, Y., Kreher, K.,
1568   Leigh, R., Merlaud, A., Mount, G. H., Navarro, M., Oetjen, H., Pazmino, A., Perez-Camacho, M., Peters,
1569   E., Pinardi, G., Puentedura, O., Richter, A., Schönhardt, A., Shaiganfar, R., Spinei, E., Strong, K.,
1570   Takashima, H., Vlemmix, T., Vrekoussis, M., Wagner, T., Wittrock, F., Yela, M., Yilmaz, S., Boersma,
1571   F., Hains, J., Kroon, M., Piters, A., and Kim, Y. J. : Intercomparison of slant column measurements of NO_2
1572   and O_4 by MAX-DOAS and zenith-sky UV and visible spectrometers. Atmos. Meas. Tech., 3(6), 1629-
1573   1646, https://doi.org/10.5194/amt-3-1629-2010, 2010

1574

1575

1576 Ryan, R. G., Rhodes, S., Tully, M., & Schofield, R. : Surface ozone exceedances in Melbourne, Australia are
1577   shown to be under NO_x control, as demonstrated using formaldehyde: NO_2 and glyoxal: formaldehyde
1578   ratios, Sci. Total Environ., 749, 141460, https://doi.org/10.1016/j.scitotenv.2020.141460, 2020

1579

1580 Sadavarte, P., & Venkataraman, C. : Trends in multi-pollutant emissions from a technology-linked inventory for
1581   India: I. Industry and transport sectors. Atmos. Environ., 99, 353-364.
1582   doi:https://doi.org/10.1016/j.atmosenv.2014.09.081, 2014
1583

1584 Sarmah, S., Singha, M., Wang, J., Dong, J., Burman, P. K. D., Goswami, S., Ge. Y., Ilyas, S., & Niu, S. :
1585   Mismatches between vegetation greening and primary productivity trends in South Asia–A satellite
1586   evidence. Int. J. Appl. Eath Obs., 104, 102561. doi:https://doi.org/10.1016/j.jag.2021.102561, 2021
1587

1588

1589 Schindlbacher, A., Zechmeister-Boltenstern, S., & Butterbach-Bahl, K. : Effects of soil moisture and temperature
1590   on NO, NO_2, and N_2O emissions from European forest soils. J. Geophys. Res., 109(D17),
1591   https://doi.org/10.1029/2004JD004590, 2004

1592

1593 Schroeder, J. R., Crawford, J. H., Fried, A., Walega, J., Weinheimer, A., Wisthaler, A., Muller, M., Mikovinu, T.,
1594   Chen,G., Shook, M. : New insights into the column CH_2O/NO_2 ratio as an indicator of near-surface ozone
1595   sensitivity. J.Geophys. Res., 122(16), 8885-8907. doi: https://doi.org/10.1002/2017JD026781,2017

1596

1597 Sharma, S., Goel, A., Gupta, D., Kumar, A., Mishra, A. , Kundu, S., Chatani, S., and Klimont, Z. : Emission
1598   inventory of non-methane volatile organic compounds from anthropogenic sources in India. Atmos.
1599   Environ., 102, 209-219. doi:https://doi.org/10.1016/j.atmosenv.2014.11.070, 2015

1600

1601

1602

1603 Seco, R., Penuelas, J., and Filella, I. : Short-chain oxygenated VOCs: Emission and uptake by plants and
1604   atmospheric sources, sinks, and concentrations, Atmos. Environ., 41(12), 2477-2499,
1605   https://doi.org/10.1016/j.atmosenv.2006.11.029, 2007

1606

1607

1608

1609 Sekiya, T., & Sudo, K. : Roles of transport and chemistry processes in global ozone change on interannual and
1610   multidecadal time scales. J. Geophys. Res., 119(8), 4903-4921.
1611   doi:https://doi.org/10.1002/2013JD020838, 2014

1612

1613 Sekiya, T., Miyazaki, K., Ogochi, K., Sudo, K., & Takigawa, M. : Global high-resolution simulations of
1614   tropospheric nitrogen dioxide using CHASER V4.0. *Geosci. Model Dev., 11*(3), 959-988.
1615   http://doi.org/10.5194/gmd-11-959-2018, 2018

1616

1617 Seinfeld, J. H., & Pandis, S. N. : Atmospheric chemistry and physics: from air pollution to climate change: John
1618   Wiley & Sons, New York, 1998

1619

1620 Sindelarova, K., Markova, J., Simpson, D., Huszar, P., Karlicky, J., Darras, S., & Granier, C. : High-resolution
1621   biogenic global emission inventory for the time period 2000–2019 for air quality modelling. *Earth Syst.*
1622   *Sci. Data, 14*(1), 251-270. doi:https://doi.org/10.5194/essd-14-251-2022, 2022
1623

1624 Singh, H., Salas, L., Chatfield, R., Czech, E., Fried, A., Walega, J., Evans, M.J., Field, B.D., Jacob, D.J., Blake,
1625   D., Heikes, B., Talbolt, R., Sachse, G., Crawford, J.H., Avery, M.A., Sandholm, S., and Fuelberg, H. :
1626   Analysis of the atmospheric distribution, sources, and sinks of oxygenated volatile organic chemicals based
1627   on measurements over the Pacific during TRACE-P, J. Geophys. Res., 109(D15),
1628   https://doi.org/10.1029/2003JD003883, 2004

1629

1630 Sinreich, R., Frieß, U., Wagner, T., and Platt, U. : Multi axis differential optical absorption spectroscopy (MAX-
1631 DOAS) of gas and aerosol distributions, Faraday discuss., 130, 153-164,
1632 https://doi.org/10.1039/B419274P, 2005

1633
1634
1635 Solomon, S., Portmann, R., Sanders, R., Daniel, J., Madsen, W., Bartram, B., and Dutton, E. : On the role of
1636 nitrogen dioxide in the absorption of solar radiation, J. Geophys. Res., 104(D10), 12047-12058,
1637 https://doi.org/10.1029/1999JD900035, 1999

1638
1639
1640 Souri, A. H., Nowlan, C. R., Wolfe, G. M., Lamsal, L. N., Miller, C. E. C., Abad, G. G., Janz, S., Fried, A., Blake,
1641 D. R., Weinheimer, A. J. , Diskin, G.S., Liu, X., and Chance, K. : Revisiting the effectiveness of
1642 HCHO/NO$_2$ ratios for inferring ozone sensitivity to its precursors using high resolution airborne remote
1643 sensing observations in a high ozone episode during the KORUS-AQ campaign. Atmos. Environ., 224,
1644 117341, https://doi.org/10.1016/j.atmosenv.2020.117341, 2020

1645
1646
1647 Sudo, K., & Akimoto, H. (2007). Global source attribution of tropospheric ozone: Long-range transport from
1648 various source regions. J. Geeophys. Res., 112(D12), https://doi.org/10.1029/2006JD007992, 2007

1649
1650 Sudo, K., Takahashi, M., Kurokawa, J., & Akimoto, H. : CHASER: A global chemical model of the troposphere
1651 1. Model description. J. Geophys. Res., 107, 4339, https://doi.org/10.1029/2001JD001113, 2002

1652
1653 Surl, L., Palmer, P. I., & González Abad, G. : Which processes drive observed variations of HCHO columns over
1654 India? Atmos. Chem. Phys., 18(7), 4549-4566 ,https://doi.org/10.5194/acp-18-4549-2018, 2018

1655
1656
1657 Takemura, T., Nozawa, T., Emori, S., Nakajima, T. Y., & Nakajima, T. : Simulation of climate response to aerosol
1658 direct and indirect effects with aerosol transport-radiation model. J. Geophys. Res., 110(D2),
1659 https://doi.org/10.1029/2004JD005029, 2005

1660

1661 Takemura, T., Egashira, M., Matsuzawa, K., Ichijo, H., O'ishi, R., & Abe-Ouchi, A. : A simulation of the global
1662   distribution and radiative forcing of soil dust aerosols at the Last Glacial Maximum. Atmos. Chem. Phys.,
1663   9(9), 3061-3073, https://doi.org/10.5194/acp-9-3061-2009, 2009

1664

1665 Tonnesen, G. S., & Dennis, R. L. (2000). Analysis of radical propagation efficiency to assess ozone sensitivity to
1666   hydrocarbons and NO_x: 1. Local indicators of instantaneous odd oxygen production sensitivity. J.Geophys.
1667   Res., 105(D7), 9213-9225. doi:https://doi.org/10.1029/1999JD900371
1668

1669

1670 Vandaele, A., C. Hermans, P. Simon, M. Van Roozendael, J. Guilmot, M. Carleer, and R. Colin.: Fourier
1671   transform measurement of NO2 absorption cross-section section in the visible range at room temperature,
1672   J. Atmos. Chem., 25(3), 289-305, doi:10.1007/BF00053797, 2009

1673

1674

1675 Vandaele, A. C., C. Fayt, F. Hendrick, C. Hermans, F. Humbled, M. V. Roozendael, M. Gil, M. Navarro, O.
1676   Puentedura, M. Yela, G. Braathen, K. Stebel, K. Tornkvist, P. Jhonston, K. Kreher, F. Goutail, F. Mieville,
1677   J.P. Pommereau, S. Khaikine, A. Richter, H. Oetjen, F. Wittrock, S. Bugarski, U. Friess, K. Pfeilsticker,
1678   R. Sinreich, T. Wagner, G. Corlett, and R. Leigh), An intercomparison campaign of ground-based UV-
1679   visible measurements of NO_2, BrO, and OClO slant columns Methods of analysis and results for NO_2, J.
1680   Geophys Res, 110(D8),2005

1681

1682

1683 Vigouroux, C., Hendrick, F., Stavrakou, T., Dils, B., De Smedt, I., Hermans, C., Merlaud, A., Scolas, F., Senten,
1684   C., Vanhaelewyn, G., Fally, S., Carleer, M., Metzger, J.-M., Müller, J.-F., Van Roozendael, M., and De
1685   Mazière, M.: Ground-based FTIR and MAX-DOAS observations of formaldehyde at Réunion Island and
1686   comparisons with satellite and model data, Atmos. Chem. Phys., 9(24), 9523-9544,
1687   https://doi.org/10.5194/acp-9-9523-2009, 2009

1688

1689

1690

1691

1692 Wagner, T., Dix, B. v., Friedeburg, C. v., Frieß, U., Sanghavi, S., Sinreich, R., & Platt, U. : MAX-DOAS O4
1693   measurements: A new technique to derive information on atmospheric aerosols—Principles and
1694   information content. J. Geophys. Res., 109(D22). doi: https://doi.org/10.1029/2004JD004904, 2004

1696 Wagner, T., Burrows, J., Deutschmann, T., Dix, B., Friedeburg, C. v., Frieß, U., Iwabuchi, H. , Hendrick, F., Heue,
1697   K.-P., Irie, H., Iwabuchi, H., Kanaya, Y., Keller, J., McLinden, C. A., Oetjen, H., Palazzi, E., Petritoli, A.,
1698   Platt, U., Postylyakov, O., Pukite, J., Richter, A., van Roozendael, M., Rozanov, A., Rozanov, V., Sinreich,
1699   R., Sanghavi, S., and Wittrock, F. : Comparison of box-air-mass-factors and radiances for Multiple-Axis
1700   Differential Optical Absorption Spectroscopy (MAX-DOAS) geometries calculated from different
1701   UV/visible radiative transfer models. Atmos. Chem. Phys., 7(7), 1809-1833.
1702   doi:https://doi.org/10.5194/acp-7-1809-2007, 2007

1705 Wang, T., Hendrick, F., Wang, P., Tang, G., Clémer, K., Yu, H., Fayt, C., Hermans, C., Gielen, C., Müller, J.-F.,
1706   Pinardi, G., Theys, N., Brenot, H., and Van Roozendael, M. : Evaluation of tropospheric SO_2 retrieved
1707   from MAX-DOAS measurements in Xianghe, China. Atmos. Chem. Phys., 14(20), 11149-11164,
1708   https://doi.org/10.5194/acp-14-11149-2014, 2014

1713 Wesely, M. : Parameterization of surface resistances to gaseous dry deposition in regional-scale numerical models.
1714   Atmos. Environ., 41, 52-63. https://doi.org/10.1016/j.atmosenv.2007.10.058, 1989

1716 Williams, J. E., Boersma, K. F., Sager, P. L., & Verstraeten, W. W,. The high-resolution version of TM5-MP for
1717   optimized satellite retrievals: description and validation. Geosci. Model Dev., 10(2), 721-750.
1718   doi:https://doi.org/10.5194/gmd-10-721-2017,2017

1721 Wittrock, F., Oetjen, H., Richter, A., Fietkau, S., Medeke, T., Rozanov, A., and Burrows, J. : MAX-DOAS
1722   measurements of atmospheric trace gases in Ny-Ålesund-Radiative transfer studies and their application,
1723   Atmos. Chem. Phys., 4(4), 955-966, https://doi.org/10.5194/acp-4-955-2004, 2004

1724

1725

1726 Woo, J-H., Kim, Y. , Kim, H-K., Choi, K-C., Eum, J-H., Lee, J-B., Lim, J-H., Kim,J., and Seong, M. : Development
1727   of the CREATE inventory in support of integrated climate and air quality modeling for Asia. Sustainability,
1728   12(19), 7930. doi:https://doi.org/10.3390/su12197930, 2020

1729

1730

1731

1732

1733